Electronic Supplementary Information

Achieving Stable Lithium Metal Anodes via the Synergistic of Electrostatic Shielding and High Li^+ Flux Inorganic Interphase

Jiangtao Yu,[1,†] Xinyu Ma,[1,†] Xiuyang Zou,[2] Yin Hu,[1] Mingchen Yang,[1] Jinhua Yang,[1] Shipeng Sun,[1] and Feng Yan[1,3*]

[1]Jiangsu Engineering Laboratory of Novel Functional Polymeric Materials, Laboratory of Advanced Negative Carbon Technologies, Suzhou Key Laboratory of Soft Material and New Energy, College of Chemistry, Chemical Engineering and Materials Science, Soochow University, Suzhou, 215123, China. E-mail: fyan@suda.edu.cn (Prof. F. Yan)

[2]School of Chemistry and Chemical Engineering, Huaiyin Normal University, No.111 West Changjiang Road, Huaian 223300, Jiangsu Province, China.

[3]State Key Laboratory for Modification of Chemical Fibers and Polymer Materials, College of Materials Science and Engineering, Donghua University, Shanghai, China.

† Authors with equal contributions.

EXPERIMENTAL SECTION

Materials

1,4,7,10-Tetraazacyclododecane (cyclen, Aladdin, 99%), allyl bromide (Aladdin, 98%), potassium carbonate (K_2CO_3, Aladdin, 99%), lithium bis(trifluoromethane sulfonyl)imide (LiTFSI, 99%), lithium hexafluorophosphate ($LiPF_6$, 99%), silver nitrate ($AgNO_3$, Sinoreagent, 99%), cyclohexyl phenyl ketone (HCPK, Aladdin, 99%), poly(ethylene glycol) diacrylate (PEGDA, Mw=200; ChemeGen, 99%), anhydrous acetonitrile (MeCN; Macklin, 99%), anhydrous ether (qschem, 99%), n-methylpyrrolidone (NMP, moisture content less than 50 ppm; Aladdin, 99%) and dimethyl sulfoxide (DMSO, moisture content less than 50 ppm; Aladdin, 99%) were used without further purification. $LiCoO_2$ (LCO), $LiNi_{0.8}Co_{0.1}Mn_{0.1}O_2$ (NCM811), polyvinylidene difluoride (PVDF-5130), black carbon was purchased from MTI Kejing Group and dried at 100 °C for 24 h before use. Electrolytes 1M LiTFSI in DME: DOL=1:1 Vol% with 1% $LiNO_3$ (LS-002) and 1M $LiPF_6$ in DMC:EC: EMC=7:2:1 Vol% (LB-003) were purchased from DuoDuo Co.

Synthesis of 1,1,4,4,7,7,10,10-octaallyltetraazacyclodecane nitraat (OTA-NO_3).

Firstly, cyclen (1.72 g, 10 mmol), allyl bromide (10.89 g, 90 mmol), and K_2CO_3 (5.5 g, 40 mmol) were added sequentially to MeCN (120 mL) and refluxed for 4 days at 80 °C under stirring. The product brominated cyclen (product-1) was obtained after washing the reaction solution three times with anhydrous ether.

Product-1 (4.1 g, 10 mmol) was dissolved in 50 mL MeCN. Then, $AgNO_3$ (7 g, 41 mmol) was added to the product-1 solution and reacted for 24 h at room temperature under stirring. Subsequently, the reaction solution was filtered and the solvent was evaporated under reduced pressure at 40 ℃ to obtain the target product (OTA-NO_3) **(Figure S1)**.

OTA-PF_6 and OTA-TFSI was obtained by anionic exchange of product-1 with saturated aqueous solutions of $LiPF_6$ and LiTFSI salt at room temperature under stirring.

The degree of cross-linking of POTA-NO_3 polymer.

The gel fraction was used to characterize the degree of cross-linking of the polymer by using the dissolution equilibrium method. The POTA-NO_3 polymer (W_1) was immersed in 6 ml solvent, and the solution was allowed to stand for 72 h at 25 ℃. Then, the POTA-NO_3 polymer was dried until the mass was no longer altered, and the mass of the polymer was weighed (W_2). The gel fraction (crosslink degree) (Xc) of the polymer was calculated by $Xc=W_2/W_1$.

Fabrication of POTA@Li and POTA@Cu electrodes.

Firstly, 1 g OTA-NO_3, 10 mg HCPK, and 10 mg PEGDA were successively added to 5 ml anhydrous DMSO and stirred until complete dissolution to obtain a precursor solution.

The precursor solution was dropped on Li and Cu foil (16mm in diameter) with the exact measurement of 10 μL and polymerized under UV light (365 nm) for 6 h, and then dried under reduced pressure for 24 h at room temperature. As a result, a protective polymer layer (POTA-NO_3) was formed on the surface of the Li and Cu foil. All procedures were carried out in an argon gas atmosphere.

POTA-PF_6 and POTA-TFSI polymer layer were constructed by the same method on the face of the lithium metal.

Material characterization

The structural information of the substance was characterized by a Varian CP3800 Fourier transform infrared (FTIR) spectrometer instrument spectrum and an NRS-5100 spectrometer (JASCO) Raman spectroscopy with a 532 nm diode-pumped solid-state laser. Nuclear magnetic resonance (NMR) spectroscopy was obtained with an AVANCE NEO 400MHz. Liquid chromatography quadrupole-time of flight tandem mass spectrometer (LC-QTOFMS) used Apollo II Ion Funnel ESI Electrospray Ion Source. The samples were solubilized with anhydrous acetonitrile at a concentration of 0.1 mg/ml. The surface topography and elemental distribution of electrodes were observed employing a scanning electron microscope (SEM) system (REGULUS 8230) in the high-vacuum operating mode. The thermogravimetric analysis was implemented on PerkinElmer TGA 4000 Co., Ltd. with 5 ℃ min^{-1}. Differential scanning calorimetry (DSC) of the POTA-NO_3 protective layer was performed using a DSC

4000 via scanning at 5 °C min^{-1} under N_2. X-ray photoelectron spectroscopy (XPS) spectrum was obtained by using PHI 5000 Versaprobe II and the characteristic spectra of electrodes at different depths were probed by sputtering the electrodes with Ar^+ at different times (0s, 60s, 120s, 240s). The electrodes removed from the cells were cleaned 3 times with pure DME solvent to remove residual electrolytes prior to SEM and XPS testing. The electrodes were transferred by a high-sealing diverter to avoid contact of the electrodes with air.

Electrochemical measurements

Li||Li and Li||Cu batteries were obtained by assembling 2032 cells in a glove box using 50 μl LS-002 as electrolyte and Celgard 2500 as separator. LCO cathode was obtained by coating an Al foil with a slurry of 80% LCO powder, 10% PVDF, 10% carbon black, and NMP solvent and dried at 100 °C for 24h. Dried aluminium foil containing active material was rolled and stamped into 14 mm diameter discs for subsequent cell testing. The mass loading of the active material was 7.6-7.8 mg cm^{-2} and 14.1-14.3 mg cm^{-2}. NCM811 cathodes were obtained using the same method and the mass loading of the active material was 7.6-7.8 mg cm^{-2}. Lithium metal electrodes (99.95%) with a diameter of 16 mm were purchased from China Energy Lithium Co., Ltd. The thicknesses of the lithium metal electrodes were 450 μm and 50 μm for battery testing at different N/P ratios. Li||LCO and Li||NCM811 full batteries were prepared using POTA@Li and bare Li as the anode, LB-003 as the electrolyte, and Celgard 2500 as the separator to assemble the 2025-type cells. LCO and NCM811 electrodes with an electrode loadings of 7.6-7.8 mg cm^{-2} were assembled with 450 μm Li metal electrodes to evaluate the cycling stability of the battery under long term cycling. Batteries with electrode loadings of 14.1-14.3 mg cm^{-2} LCO electrodes and 50 μm Li metal electrodes were assembled to test the cycling stability of the batteries at low anodic excesses (N/P=2.49). All batteries were assembled in an argon-filled glove box (O_2<0.01 ppm, H_2O<0.01 ppm).

Linear sweep voltammetry (LSV) was used to probe the reductive decomposition potential of OTA^{4+} cations by the three-electrode method (glassy carbon as working electrode, Pt as counter electrode, and Ag/AgCl as reference electrode) from 0 to -6 V potentials and scan rate of 1mV s^{-1}. Due to the lower

reduction potential of the NO_3^- anion, the NO_3^- anion was replaced with the $TFSI^-$ anion for testing, and a 100 mM OTA-TFSI test solution was prepared using PC as the test solvent.

The electrochemical impedance spectra (EIS) of Li||Li, Li||NCM811 cells were evaluated with frequency of 0.1 Hz-1 MHz and a polarization voltage of 10 mV. The Li^+ transfer activation energy (Ea) of the Li||Li cells was calculated by the Arrhenius formula.

$$\frac{1}{R_{ct}} = A \exp(-\frac{E_a}{RT})$$

where the A was the pre-exponential factor, R_{ct} was the impedance value from the EIS test results, T was the absolute temperature, R was the molar gas constant.

The Li^+ transference number (t_{Li^+}) was calculated by AC impedance and DC polarization experiment in the Li||Li cells. The equation for calculating is shown in the Equation,

$$t_{Li^+} = \frac{I_{ss}(\Delta V - I_0 R_0)}{I_0(\Delta V - I_{ss} R_{ss})}$$

where the ΔV was polarization voltage (10 mV), I_0, I_{ss} and the R_0, R_{ss} represented the current and impedance in the initial and steady-state after 1500 seconds of polarization, respectively.

The Coulombic efficiency (CE) of Li||Cu cells was measured by Wang et al. developed the method at 2mA cm^{-2}.[1] The Cu electrode was first plated with 3 mAh cm^{-2} lithium (Q_s) and then stripped completely. Subsequently, 3 mAh cm^{-2} lithium continued to be plated on the Cu substrate, and 1 mAh cm-2 lithium (Q_c) was plated/stripped in each of the following n cycles, and finally all the lithium on the Cu electrode was stripped (Q_t). The average CE is calculated by the equation:

$$CE = \frac{nQ_C + Q_s}{nQ_C + Q_t}$$

Li||LCO and Li||NCM811 batteries were tested for charge/discharge cycling by LAND 2001A over a voltage range of 2.8-4.3 V. The Li^+ diffusion coefficient in the electrodes was conducted by galvanostatic intermittent titration technique (GITT). The test was performed by charging/discharging for 10 min and then leaving the battery for 1 h until the specified voltage was reached. The diffusion coefficient was obtained by the equation:

$$D = \frac{4}{\pi\tau}\left(\frac{n_m V_m}{S}\right)^2\left(\frac{\Delta E_s}{\Delta E_t}\right)^2$$

where τ was the relaxation time, nm is the molar fraction of the electrode, V_m was the molar volume of the electrode material, S was the contact area of the electrode with the electrolyte, ΔE_s was the change in voltage due to the pulse, and ΔE_t was the change in voltage for a constant-current charge/discharge.

Details in Molecular Dynamics Simulation

Simulations were performed using the Materials Studio package with the COMPASSII force field. The amount of electrolyte infiltration in the POTA-NO_3 polymer (LB-003 : POTA-NO_3=4.3 : 5, wt %) was characterized prior to MD simulation to guide the number of solvent molecules, lithium salts and polymer molecules in the simulation system. The system contains 10 POTA-NO_3 (20 repeat units) or not, 90 $LiPF_6$, 722 DMC, 271 EC and 98 EMC. The periodic boundary conditions were applied in the X, Y and Z directions for all systems. The simulation process was subjected to 1 ns NPT simulation (time step = 1 fs, frame output for every 5000 steps, T = 298K, P = 0.0001 GPa), followed by a 2 ns NVT equilibrium simulation (time step = 1 fs, frame output for every 10000 steps, T = 298 K). The Ewald & Group summation method was used to calculate the electrostatic interactions with an accuracy of 0.0001 kcal·mol^{-1}. In addition, the atom-based summation method was used to study the van der Waals interactions with a cutoff distance of 12.5 Å.

Modeling simulation

The deposition behavior of Li^+ on the electrodes and the evolution of Li^+ concentration during the actual operation of the battery is more complex than the model constructed in this paper. In this simplified model performed by COMSOL Multiphysics 6.0. The electrochemical deposition of Li metal was simulated through the software preset interface to the lithium-ion battery, and the kinetic expression type of the battery interface was specified as lithium metal. The mass transfer and charge conservation of Li^+ in the electrolyte were described by the Nernst-Planck equation. A square area with 2.0 × 1.0 mm^2 was set up as the study area and the current density was set to 1 mA cm^{-2}. Four semi-ellipses were set up on the electrodes as Li deposition cores. The type of body electrolyte was selected as 1 M $LiPF_6$ in EC: DMC

(1:1, Vol%). The ionic diffusion coefficients of Li^+ and PF_6^- in electrolyte were 5×10^{-7} cm^2 s^{-1} and 2×10^{-6} cm^2 s^{-1}, respectively. The deposition rate of Li^+ on the electrode is regulated by setting the exchange current density on the electrode surface. The exchange current density on the surface of bare Li electrode was set to 1 e^2 (A m^{-2}). For POTA@Li electrode, the exchange current density at the semi-ellipse was 0.05 e^2 (A m^{-2}) and 1.32 e^2 (A m^{-2}) at flat electrodes.

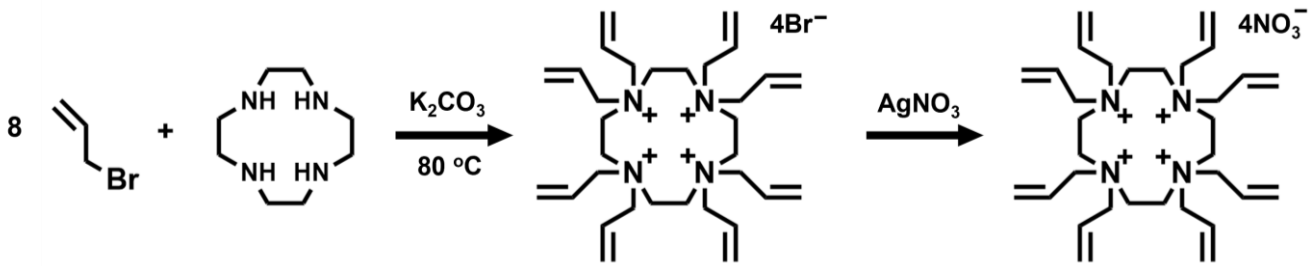

Figure S1. Synthetic route of OTA-NO_3.

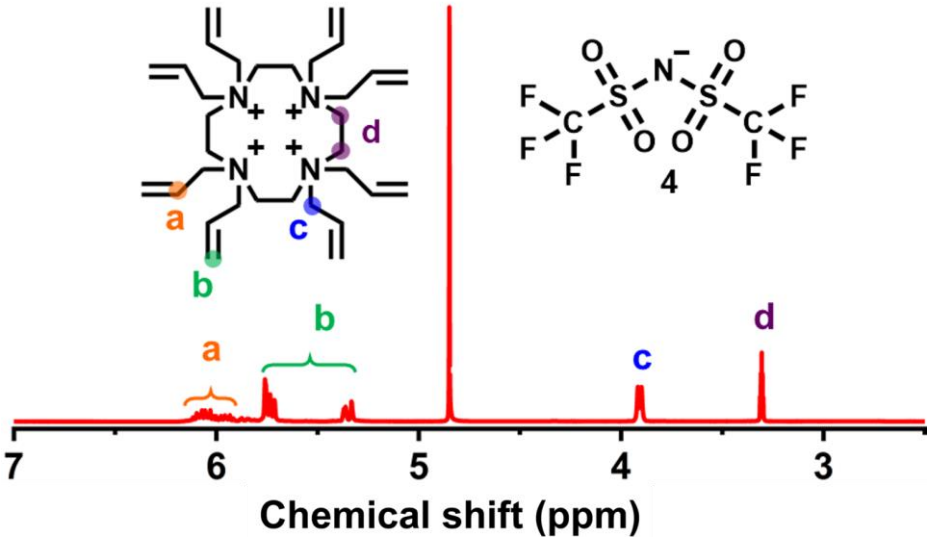

Figure S2. ^{1}H NMR spectra of OTA-TFSI.

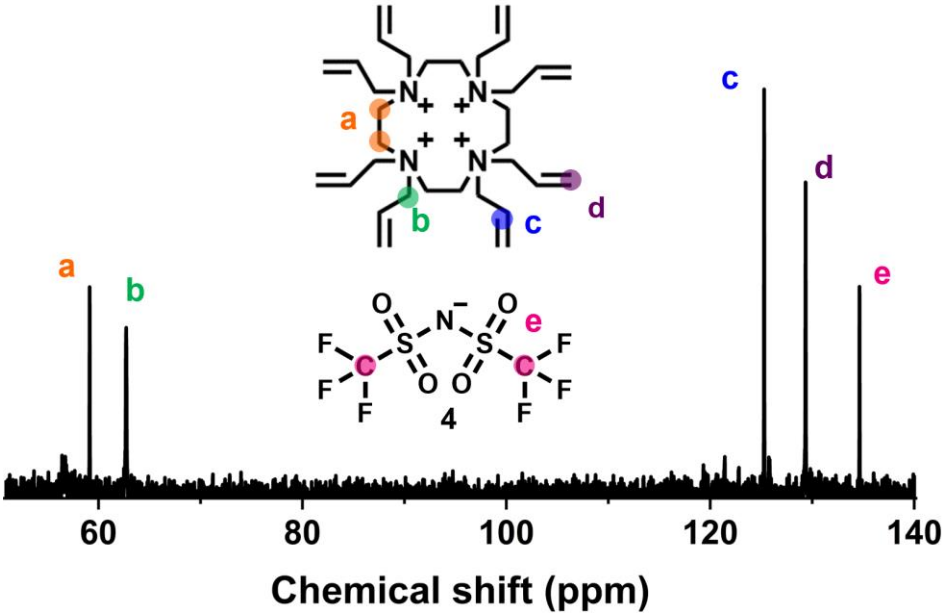

Figure S3. ^{13}C NMR spectra of OTA-TFSI.

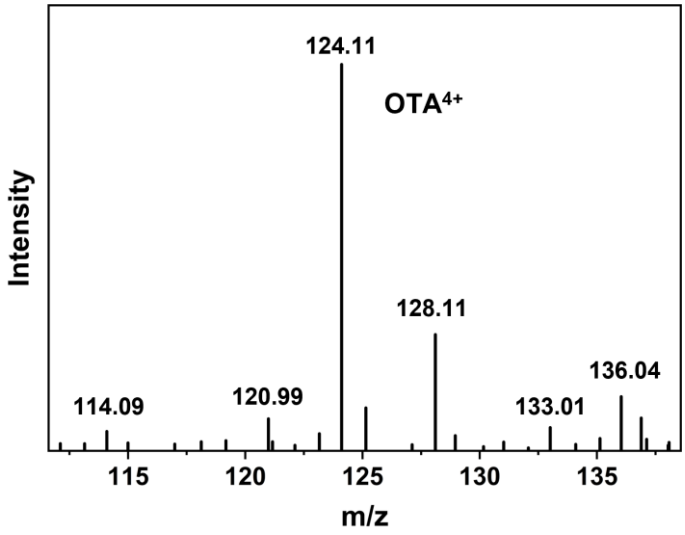

Figure S4. LC-QTOFMS for OTA-NO_3 monomer molecule.

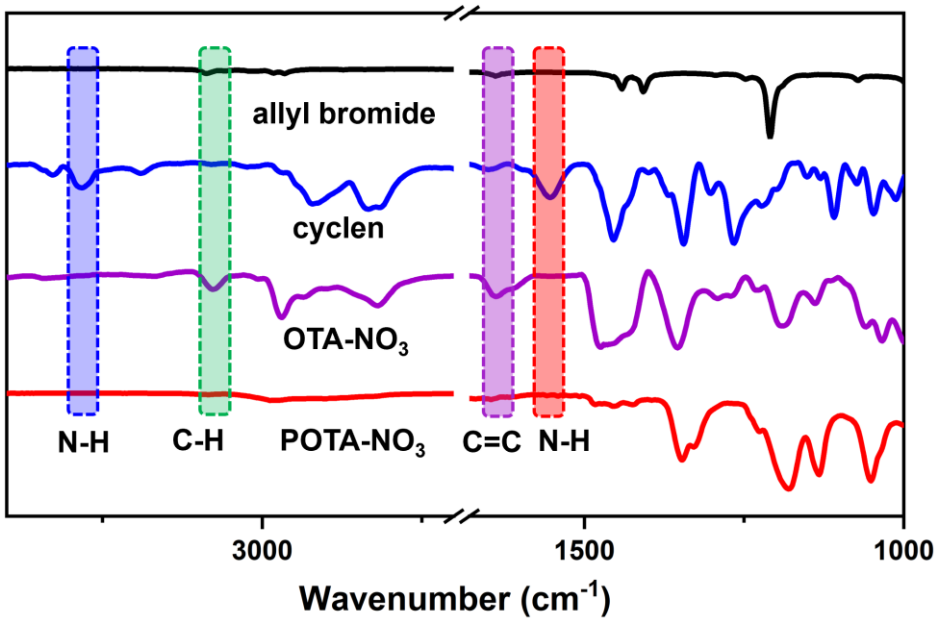

Figure S5. FTIR spectrum of allyl bromide, cyclen, OTA-NO_3, and POTA-NO_3.

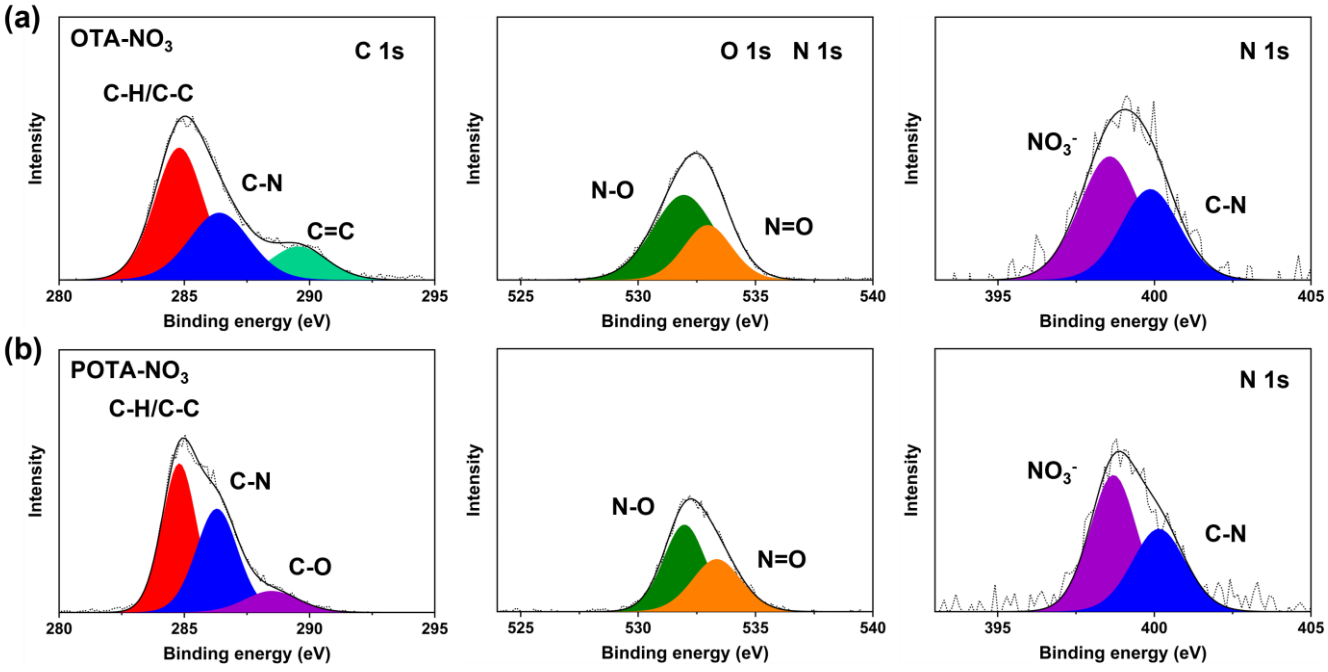

Figure S6. The XPS spectra of (a) OTA-NO_3 and (b)POTA-NO_3.

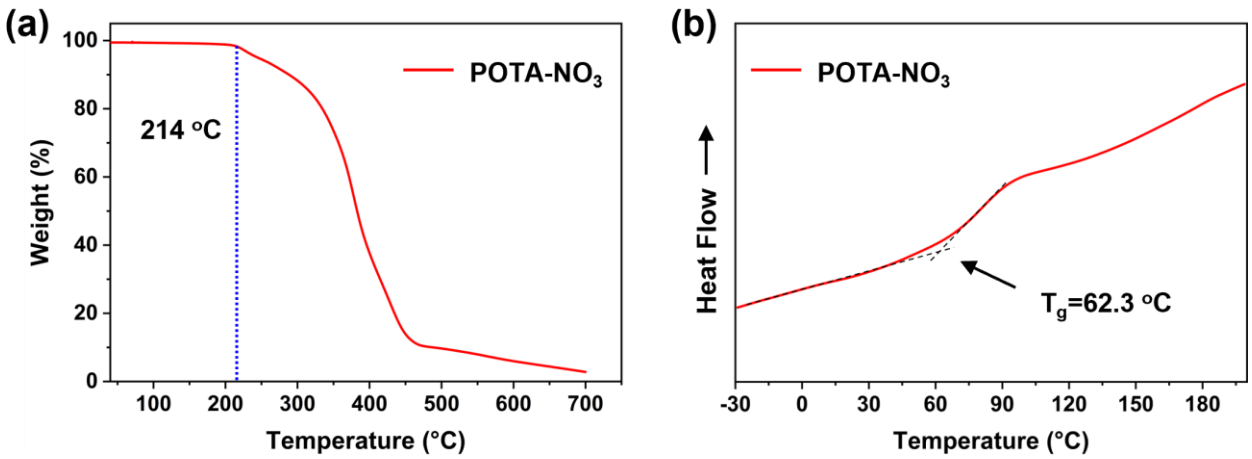

Figure S7. (a)TGA and (b)DSC of POTA-NO_3 under N_2 atmosphere, heating rate: 5 °C min^{-1}.

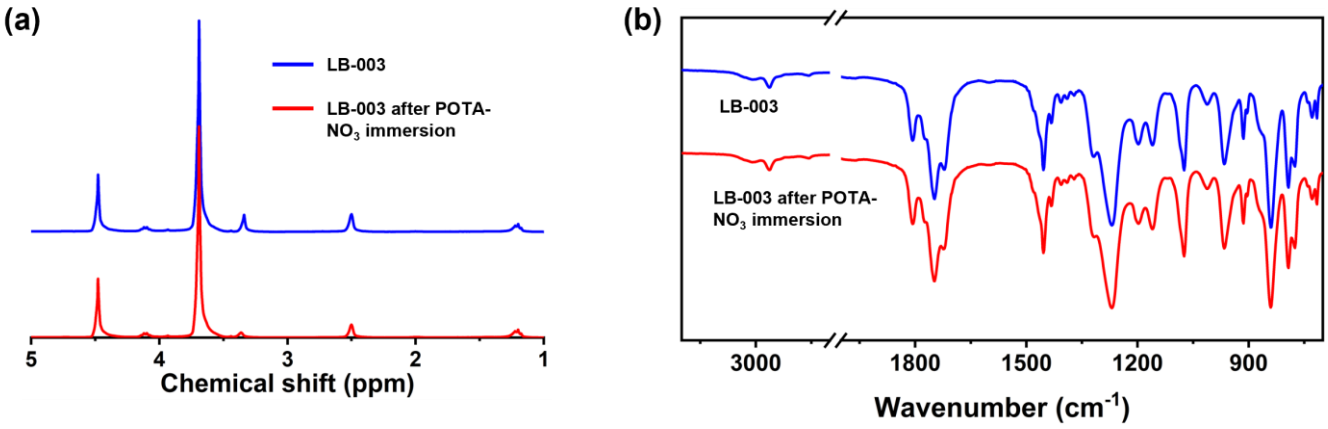

Figure S8. (a) ^1H NMR spectra and (b) FTIR spectrum of LB-003 electrolyte and LB-003 electrolyte after POTA-NO_3 immersion.

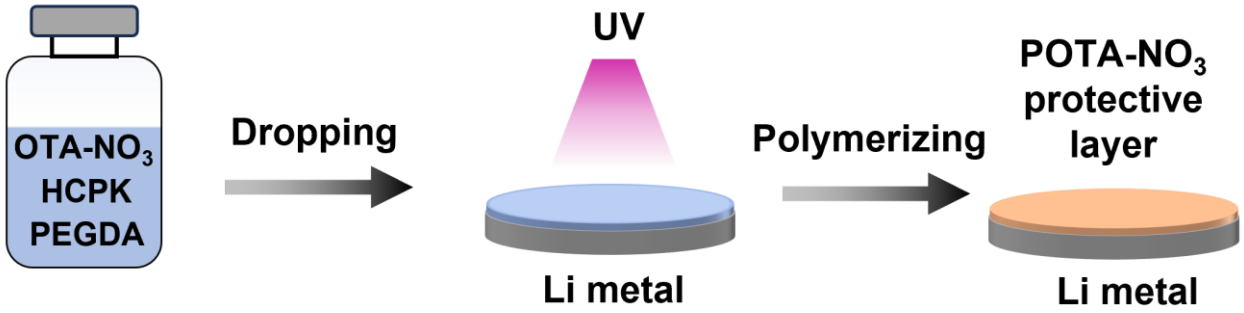

Figure S9. Schematic description for preparation procedure of POTA-NO_3 protected electrode.

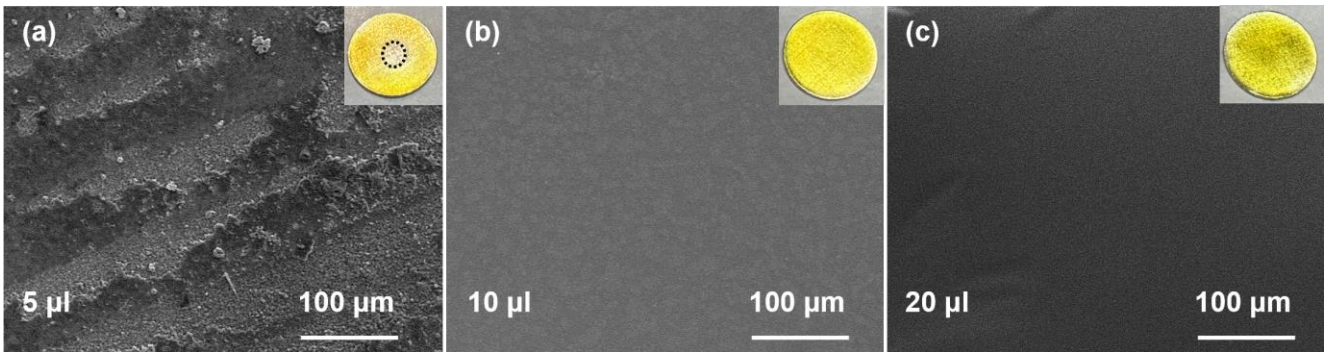

Figure S10. SEM images of POTA-NO_3 protected lithium metal with (a) 5 µL, (b) 10 µL and (c) 20 µL precursor solution dosages.

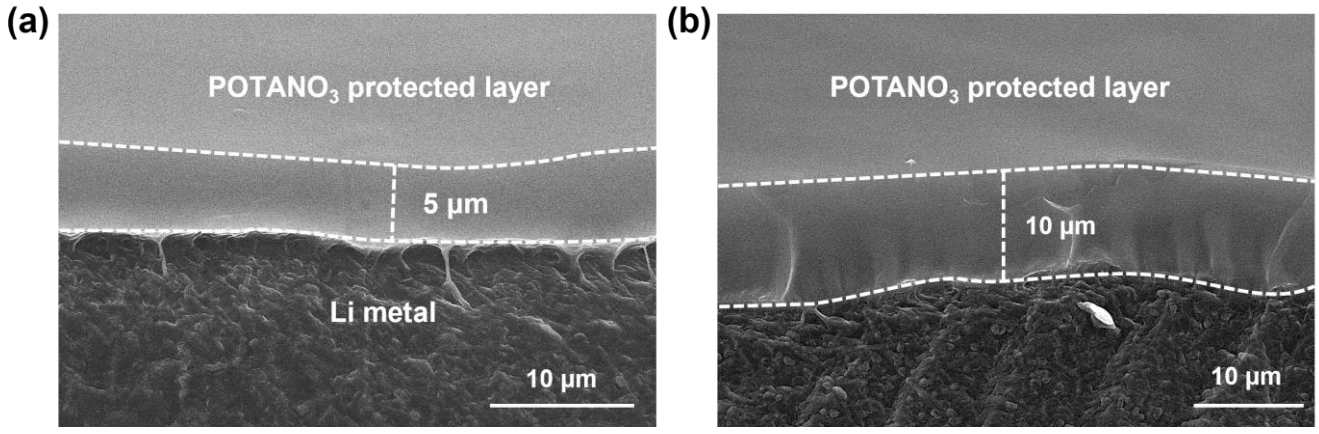

Figure S11. Cross-sectional SEM image of POTA-NO_3 protected lithium metal with (a)10 µL and (b)20 µL of precursor solution dosages.

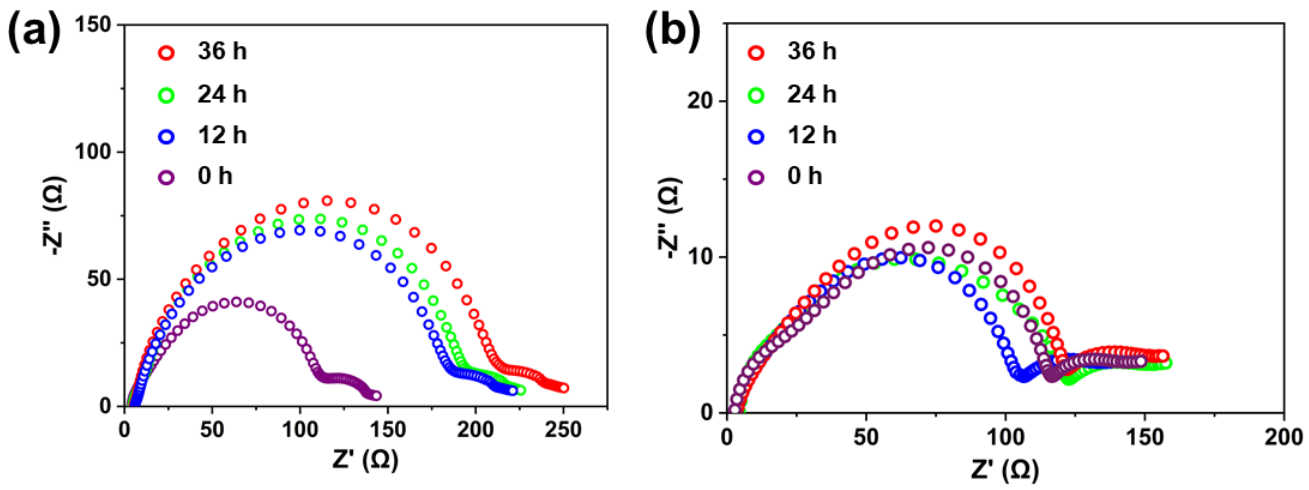

Figure S12. Resting time-dependent Nyquist plots of (a) bare Li||Li and (b) POTA@Li||POTA@Li cells. Electrolyte decomposition caused by the high reactivity of lithium metal was responsible for the change in interface impedance of bare Li||Li cells during standing.

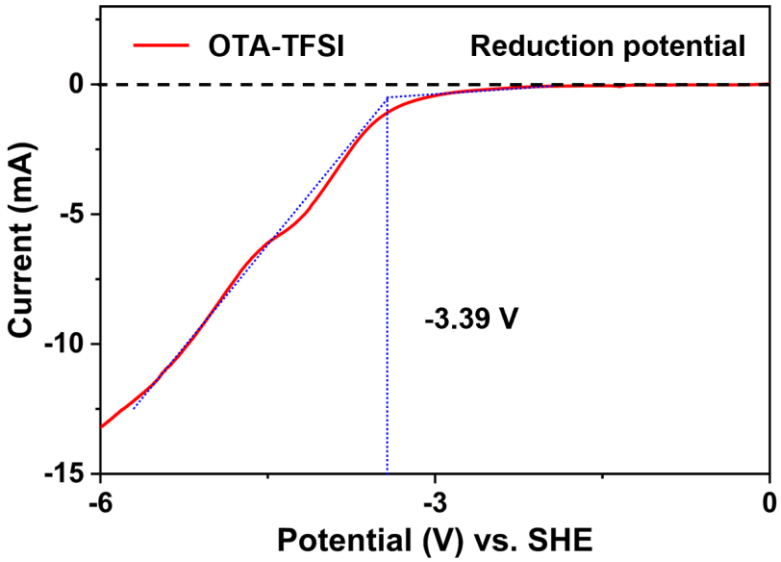

Figure S13. LSV result of monomer OTA-TFSI at 0 V to -6 V by three-electrode device. To avoid the effects of NO_3^- decomposition on the test, the NO_3^- anion in the ionic liquid was replaced with a reduction-stable $TFSI^-$ anion.

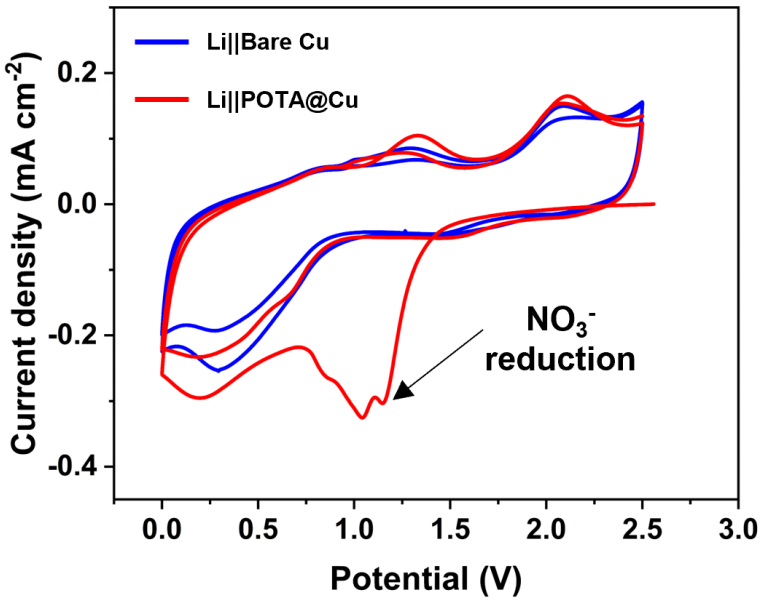

Figure S14. CV curves of Li||bare Cu and Li||POTA@Cu cells with LB-003 electrolyte in the range of 0-2.5 V at a scan rate of 0.1 mV s^{-1}.

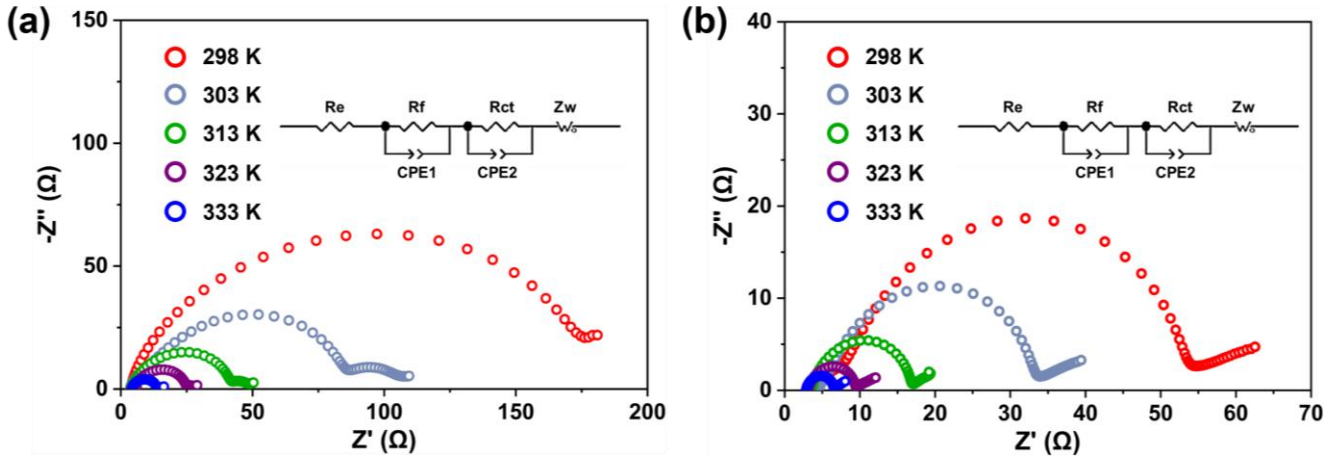

Figure S15. Temperature-dependent Nyquist plots of (a) bare Li||Li, and (b) POTA@Li||POTA@Li cells. To promote the formation of inorganic SEI derived from NO_3^- in POTA-NO_3, the EIS tests of bare Li||Li, and POTA@Li||POTA@Li cells were performed for 4 h at 1 mA $cm^{-2}$and 1 mAh cm^{-2}. The insets are corresponding equivalent circuits. The SEI resistance (R_f) and the charge transfer resistance (Rct) in Nyquist plots can be identified based on equivalent circuit fitting. The activation energy (E_a) of Li^+ pass SEI can be calculated by the Arrhenius formula.

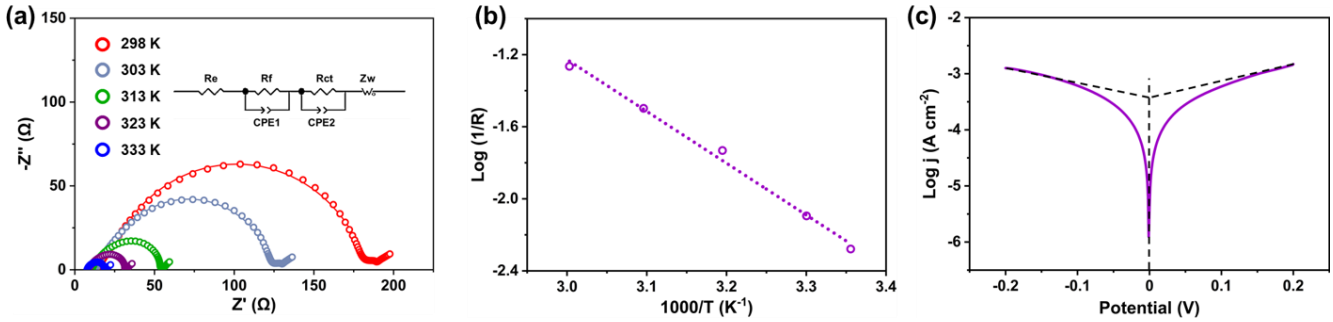

Figure S16. (a)Temperature-dependent Nyquist plots, (b) Arrhenius plots and (c) Tafel curves of Li||Li with 10 μm polymer protective coating.

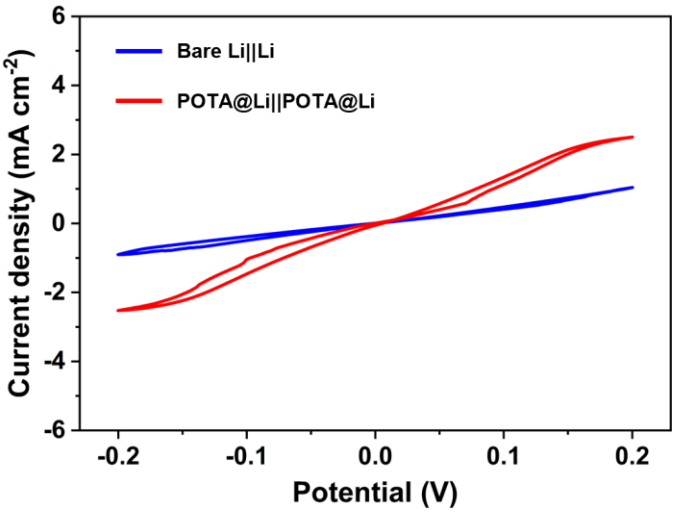

Figure S17. CV curves of bare Li||Li and POTA@Li||POTA@Li cells from −0.2 to 0.2 V at a scan rate of 1 mV s^{-1}.

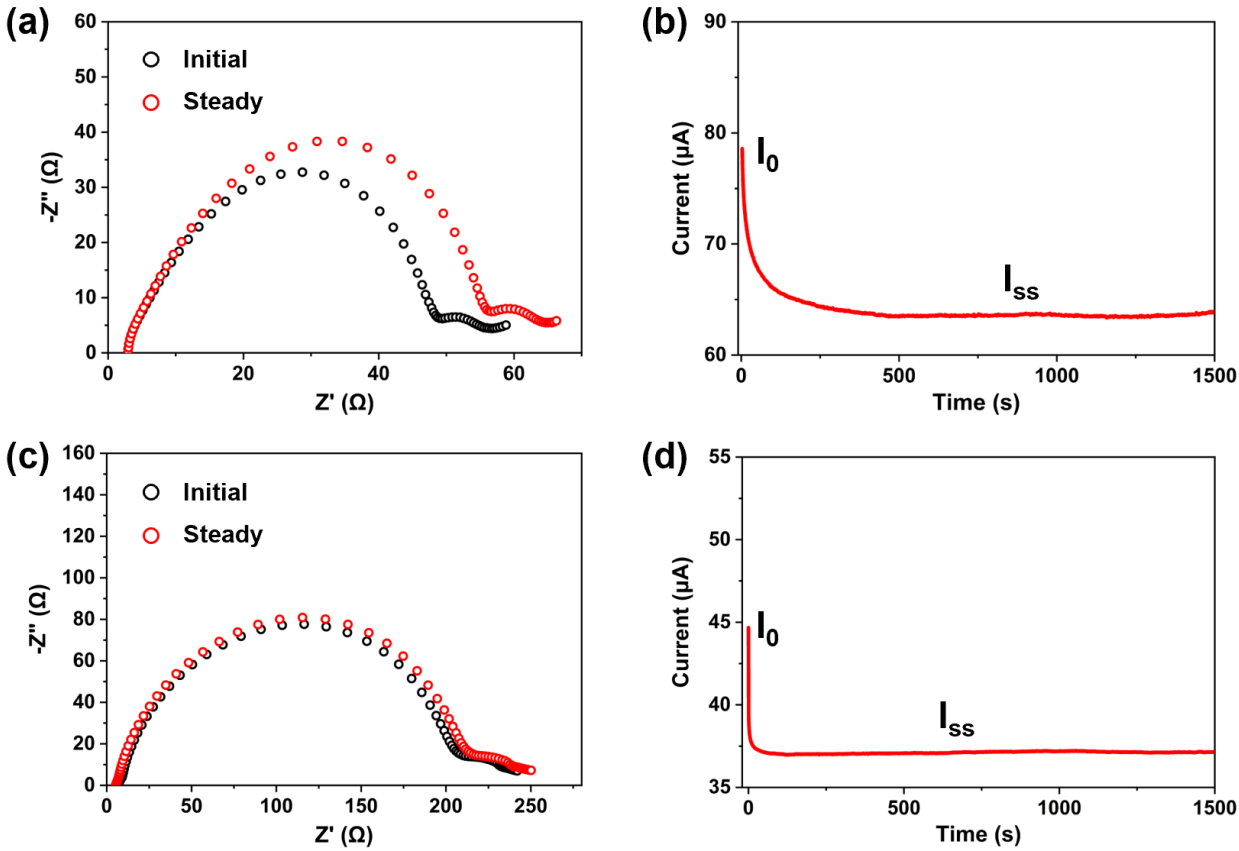

Figure S18. Nyquist plots of (a) POTA@Li||POTA@Li and (c) bare Li||Li before and after polarization and time-current polarization curves of (b) POTA@Li||POTA@Li and (d) bare Li||Li. To promote NO_3^- anion decomposition, the EIS and constant voltage polarization tests were carried out on bare Li||Li and POTA@Li||POTA@Li cells after cycling for 4 h at 1 mA cm^{-2} and 1 mAh cm^{-2}.

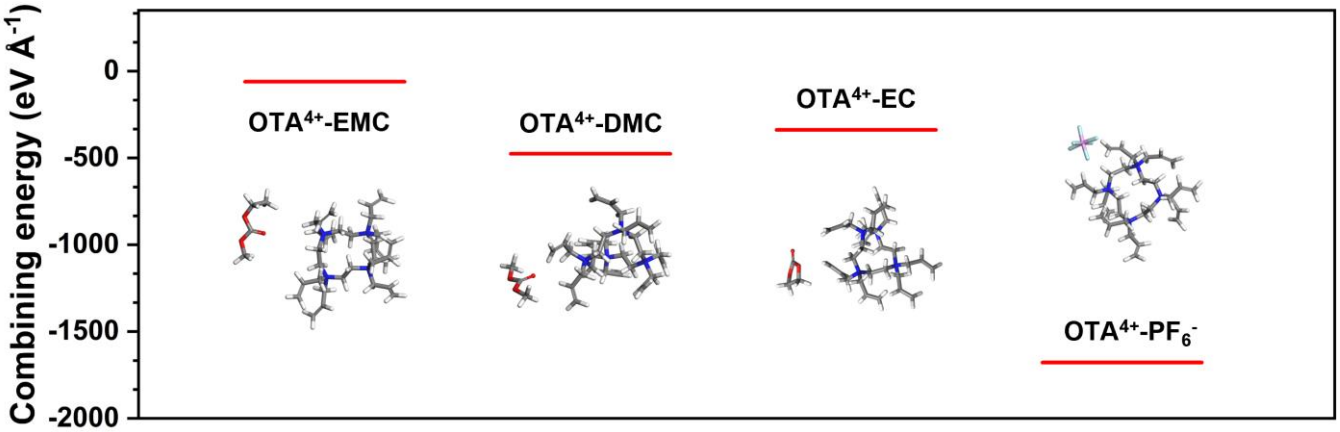

Figure S19. Combining energy of OTA^{4+} cations with carbonate molecules and PF_6^- anions.

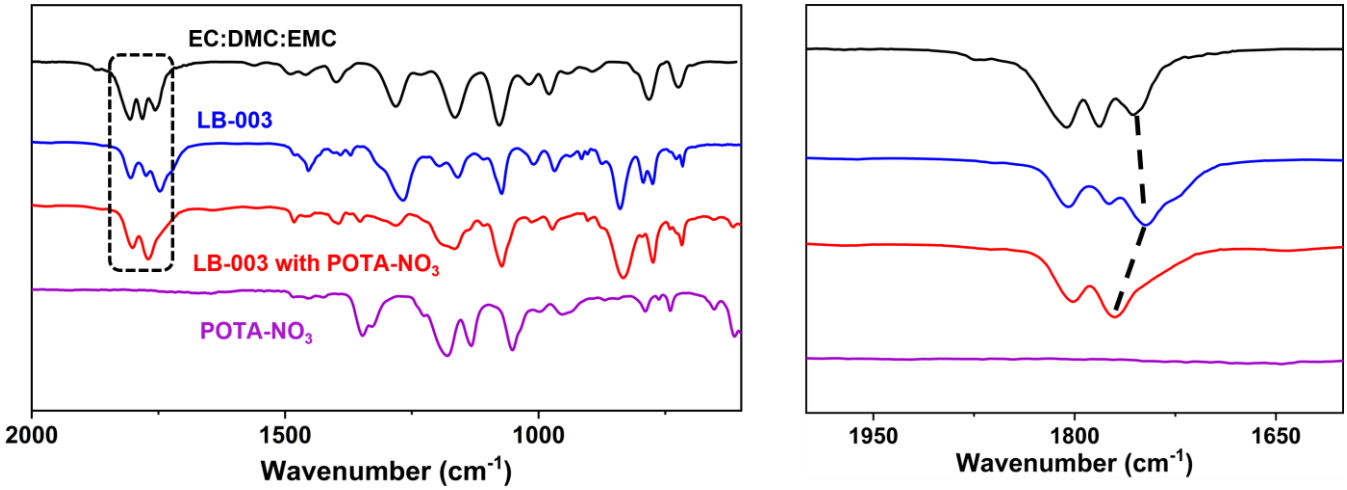

Figure S20. FTIR spectra comparison of carbonate, LB-003 and LB-003 with POTA-NO_3 polymer. Ionic dipole interactions between the Li+ and the O atoms in the carbonate solvent will affect the chemical environment of the C=O bonds and result in the weak C=O bonds, which shifts the FTIR peak down in LB-003 electrolyte. However, the C=O bond of solvent molecules shifted to higher wavenumbers in LB-003 with POTA-NO_3 compared to the LB-003 electrolyte. This discrepancy is attributed to the "tug-of-war" effect of competitive interactions between the OTA^{4+} cations and Li^+ on the carbonate solvent. The intense ionic dipole interaction between the OTA^{4+} cations and the carbonate molecule can "drag" the solvent molecule away from the Li^+, reducing the Li^+ effect on the carbonate solvent molecule. However, the ionic dipole interactions between Li^+ and solvent molecules can similarly shield the effect of OTA^{4+} cations on solvent molecules. Thus, the FTIR results of the C=O bonds in the solvent molecules in LB-003 with POTA-NO_3 are shifted to higher wavenumber than those in LB-003 electrolyte because of the interaction between OTA^{4+} and Li^+.

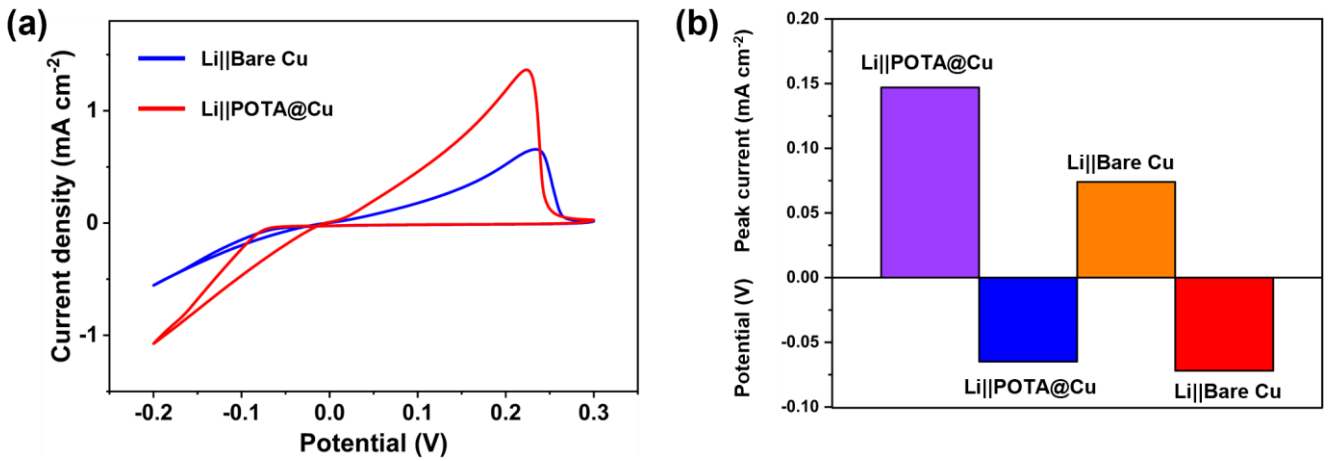

Figure S21. (a) CV curves of Li||bare Cu and Li||POTA@Cu cells in the range -0.2 V to 0.3 V at a scan rate of 0.1 mV s^{-1}. (b) Redox current density and the initial deposition potential identified from CV curves.

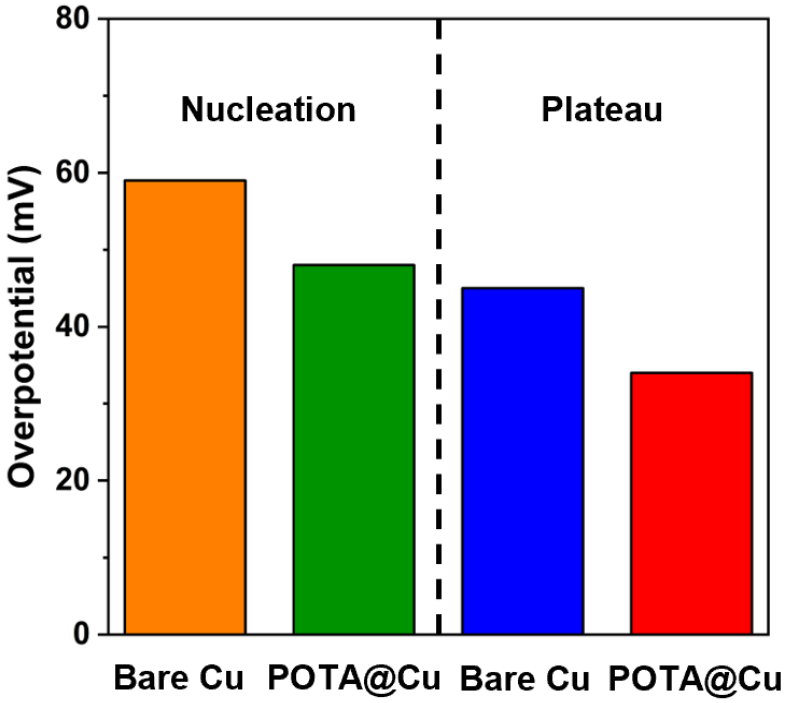

Figure S22. Li^+ nucleation and plateau potential during deposition on bare Cu and POTA@Cu electrodes identified from the Coulomb efficiency test curves of Li||Cu cells.

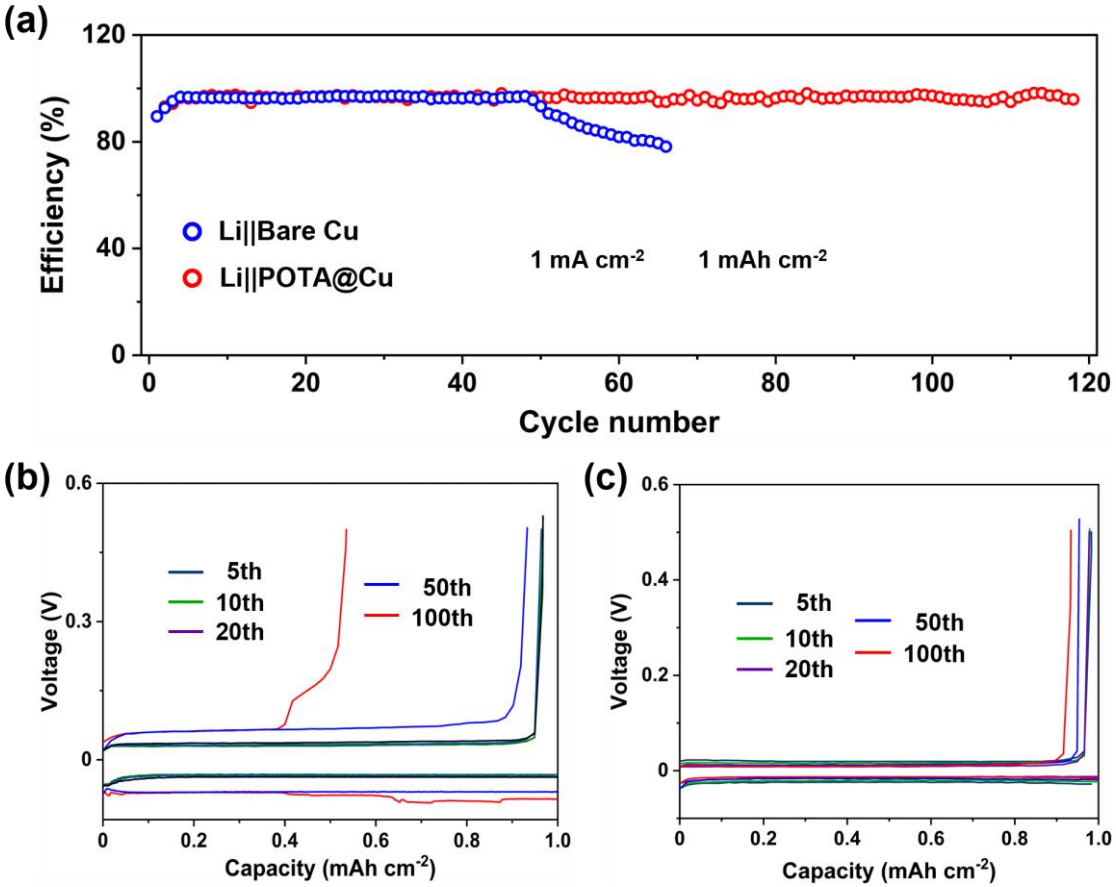

Figure S23. (a) Cycling stability of Li||bare Cu and Li||POTA@Cu cells at 1 mA cm^{-2} and 1 mAh cm^{-2}. Electrochemical characteristics of Li plating/stripping of (b) Li||bare Cu and (c) Li||POTA@Cu cells.

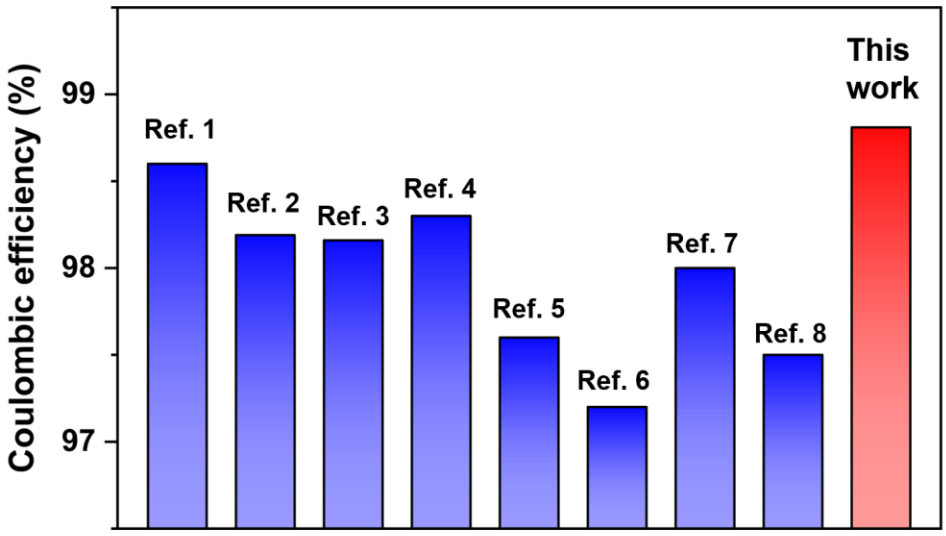

Figure S24. Comparison of Coulombic efficiency of this work with previously published literatures. [S1–S8]

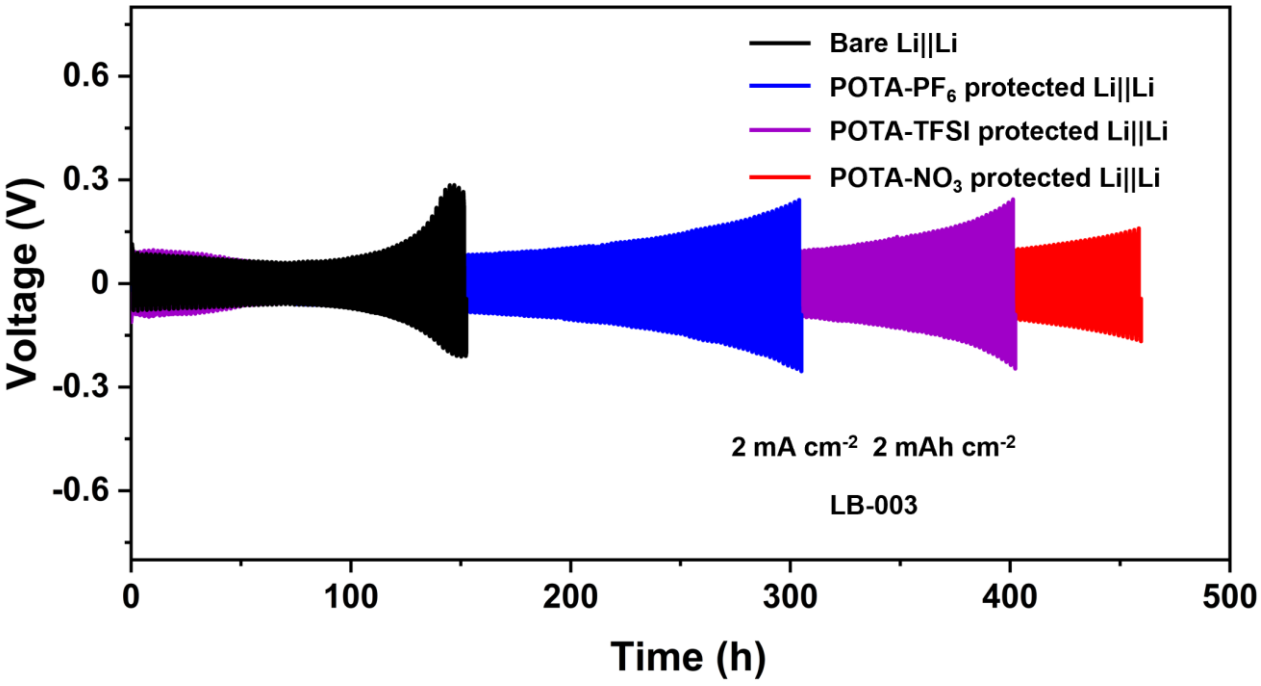

Figure S25. Voltage-time profiles of bare Li||Li, POTA-PF_6 protected Li||Li, POTA-TFSI protected Li||Li and POTA-NO_3 protected Li||Li cells at cyclic condition of 2 mA cm^{-2}, 2 mAh cm^{-2}.

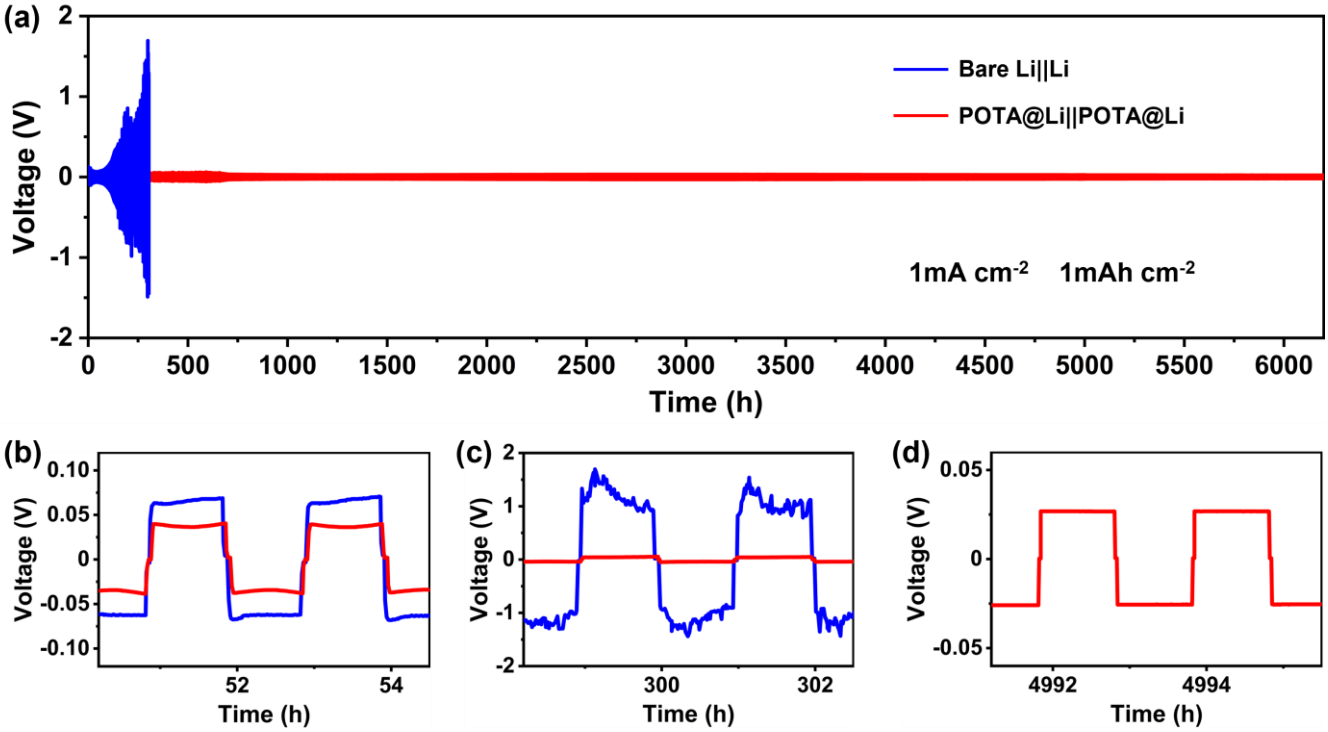

Figure S26. (a) Time-voltage polarization curves for bare Li||Li and POTA@Li||POTA@Li at 1 mA cm^{-2}, 1 mAh cm^{-2}. Voltage profile local enlarged images of (b) 51-55 h, (c) 298-303 h and (d) 4991-4995 h.

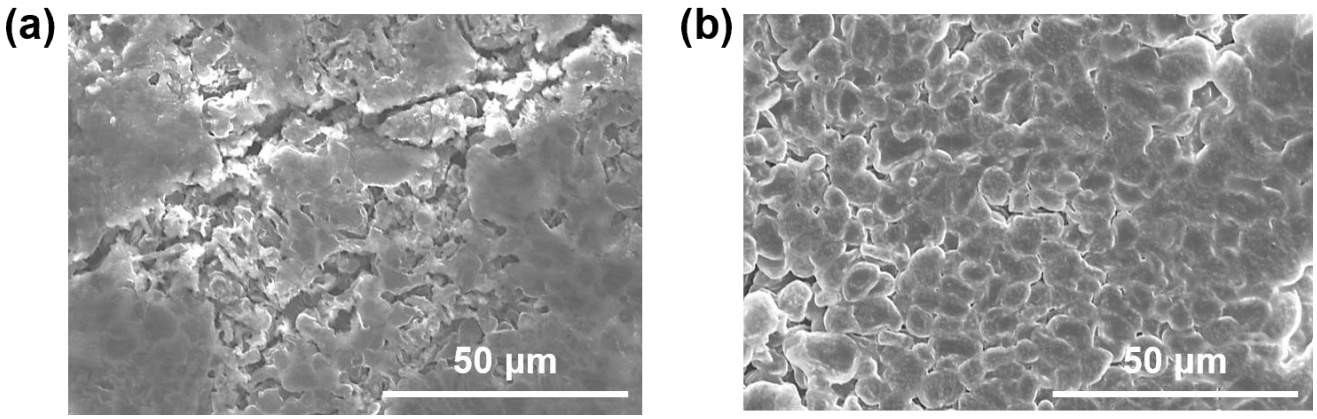

Figure S27. SEM images of (a) bare Li and (b) POTA@Li electrodes in bare Li||Li and POTA@Li||POTA@Li cells after 50 cycles at 2 mA cm^{-2} and 2 mAh cm^{-2}.

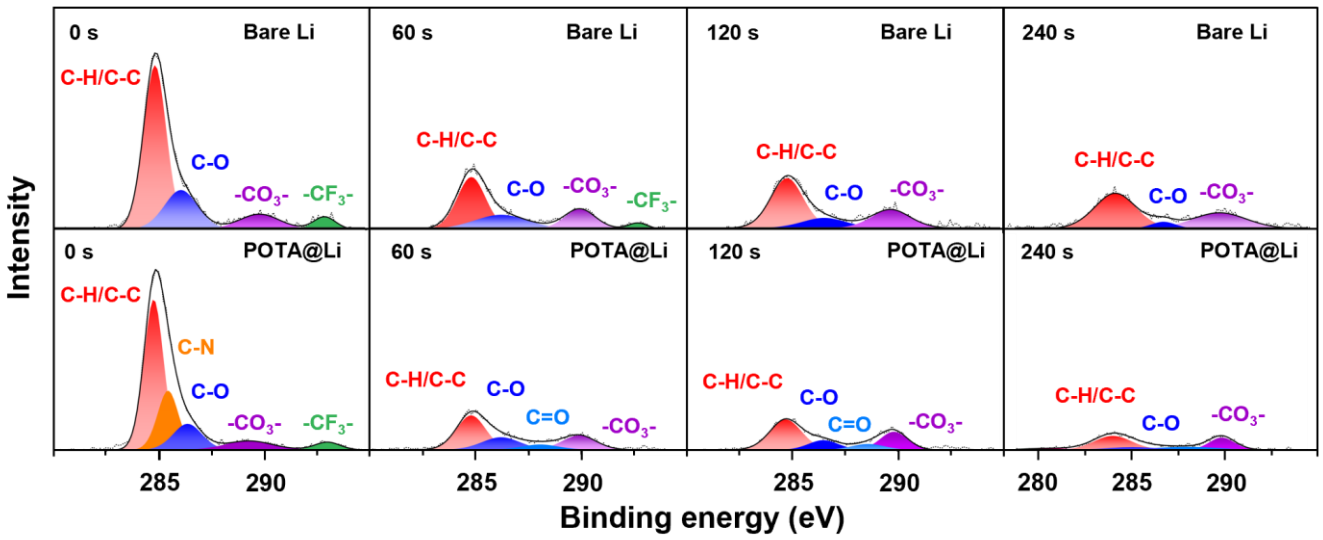

Figure S28. C1s XPS in-depth spectra of bare Li and POTA@Li electrodes in bare Li||Li and POTA@Li||POTA@Li cells after 20 cycles at 1mA cm^{-2}, 1mAh cm^{-2}.

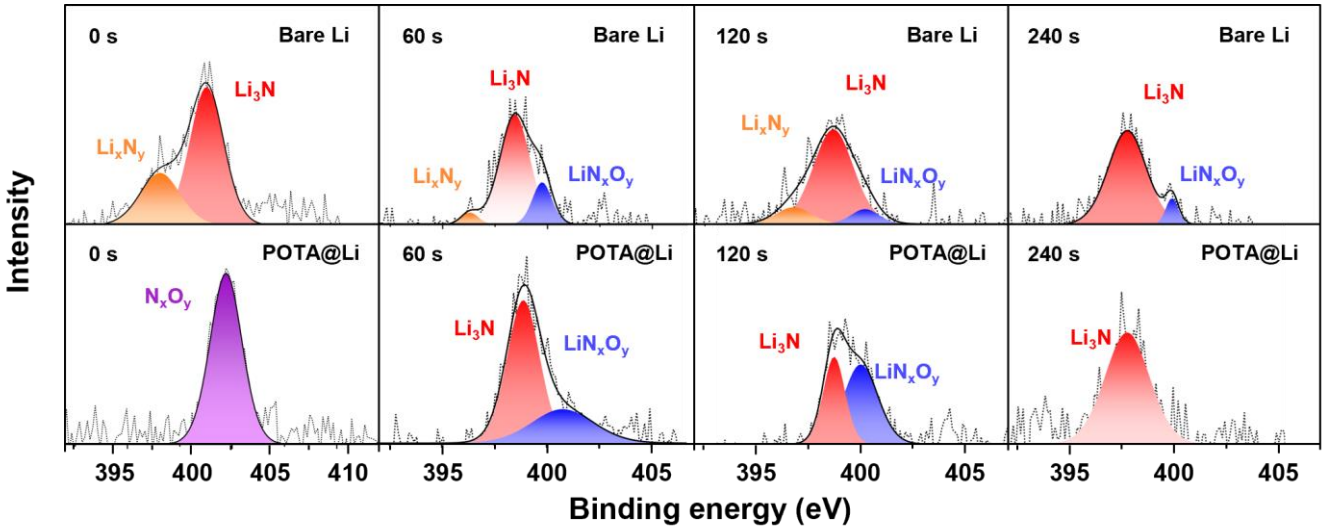

Figure S29. N1s XPS in-depth spectra of bare Li and POTA@Li electrodes in bare Li||Li and POTA@Li||POTA@Li cells after 20 cycles at 1 mA cm^{-2}, 1 mAh cm^{-2}.

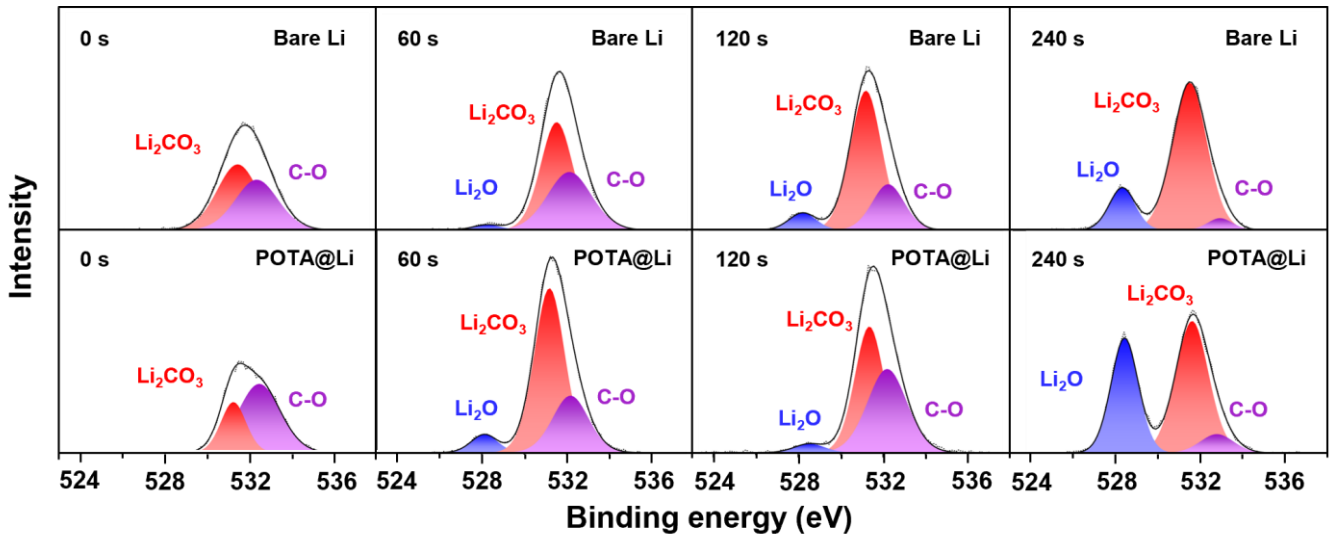

Figure S30. O1s XPS in-depth spectra of bare Li and POTA@Li electrodes after 20 cycles in bare Li||Li and POTA@Li||POTA@Li cells at 1 mA cm^{-2}, 1 mAh cm^{-2}.

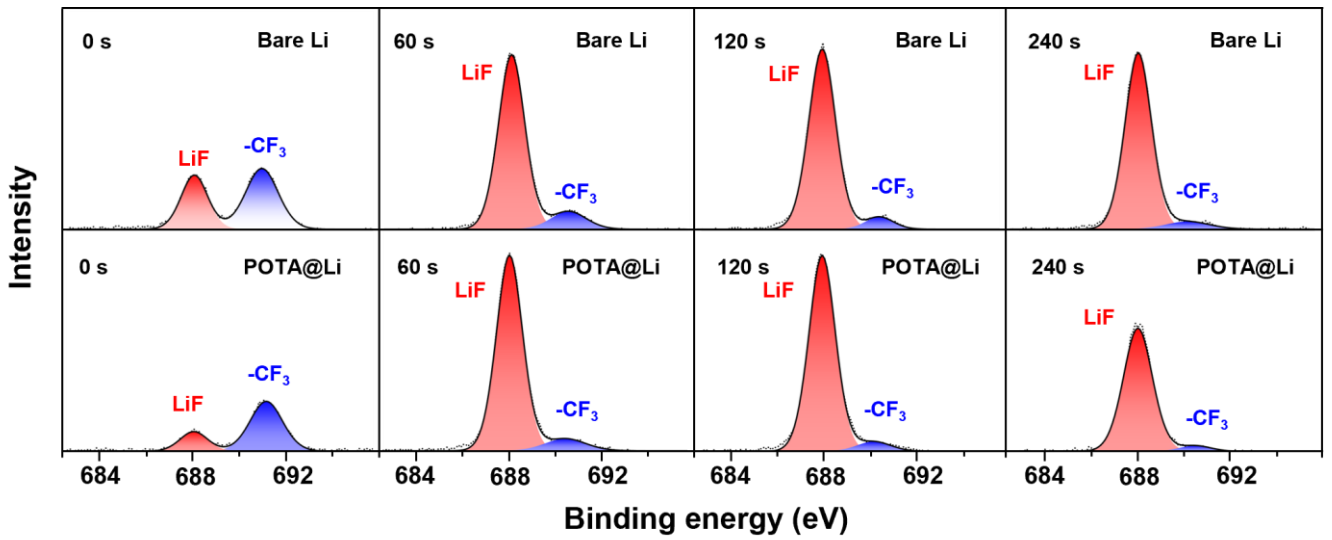

Figure S31. F1s XPS in-depth spectra of bare Li and POTA@Li electrodes after 20 cycles in bare Li||Li and POTA@Li||POTA@Li cells at 1 mA cm^{-2}, 1 mAh cm^{-2}.

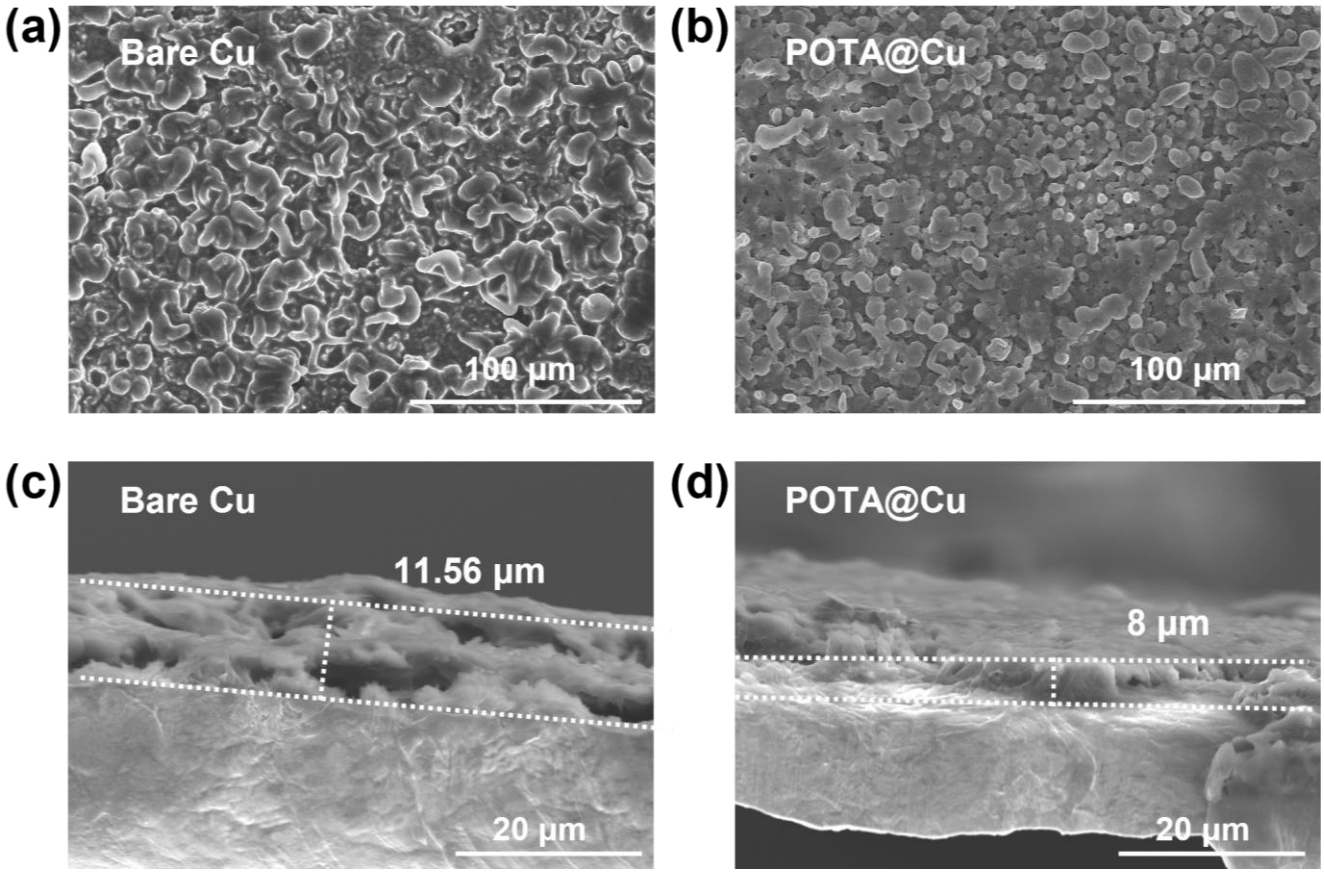

Figure S32. Top-view SEM images of (a) bare Cu and (b) POTA@Cu electrodes, and cross-sectional view of (c) bare Cu and (d) POTA@Cu electrodes after plating lithium 2 mAh cm^{-2} at current density of 0.5 mA cm^{-2}.

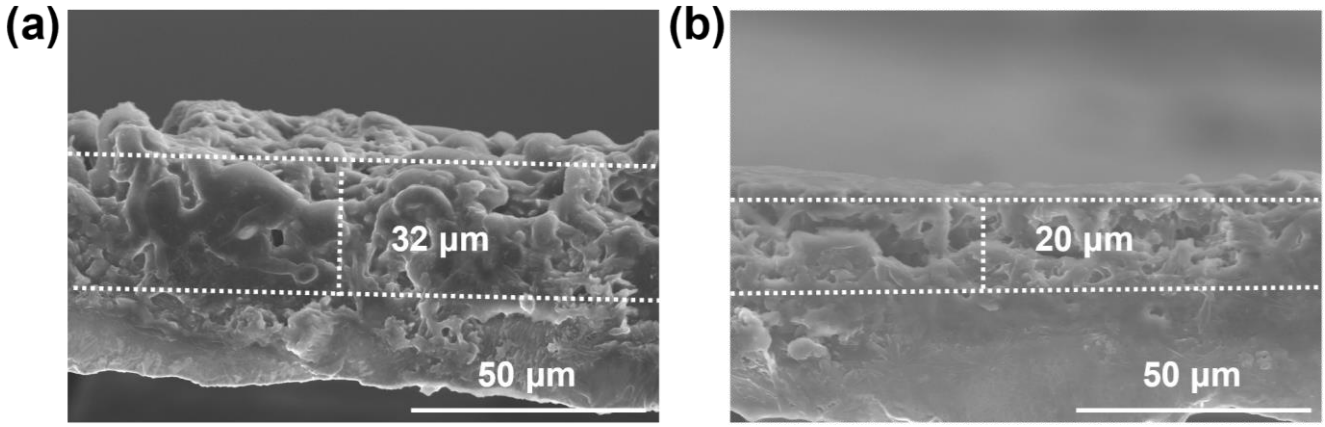

Figure S33. Cross sections morphology of (a) bare Cu and (b) POTA@Cu electrodes after lithium plating with 4 mAh cm^{-2} at current density of 0.5 mA cm^{-2}.

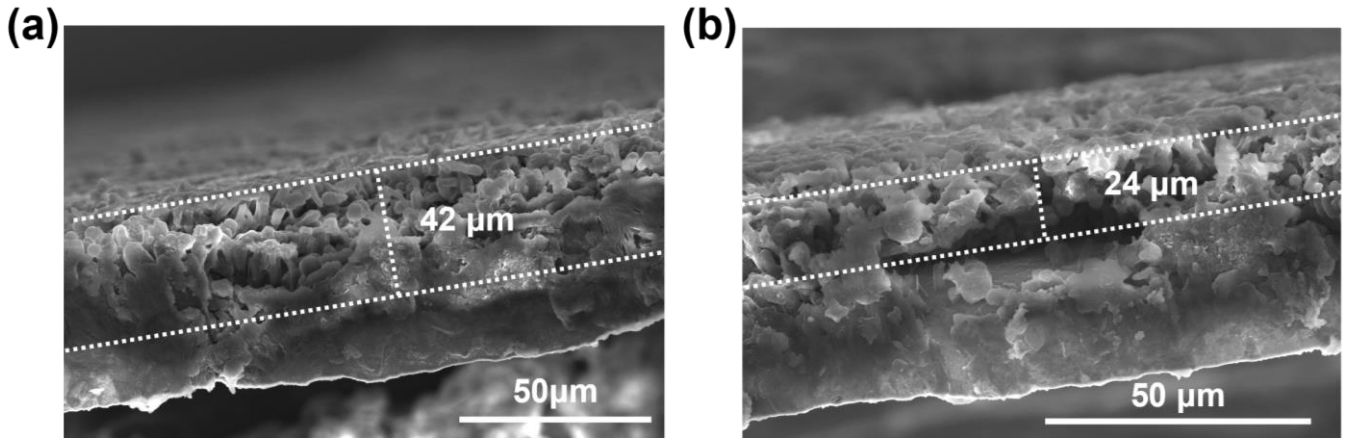

Figure S34. Cross sections morphology of (a) bare Cu and (b) POTA@Cu electrodes after lithium plating with 8 mAh cm^{-2} at current density of 0.5 mA cm^{-2}.

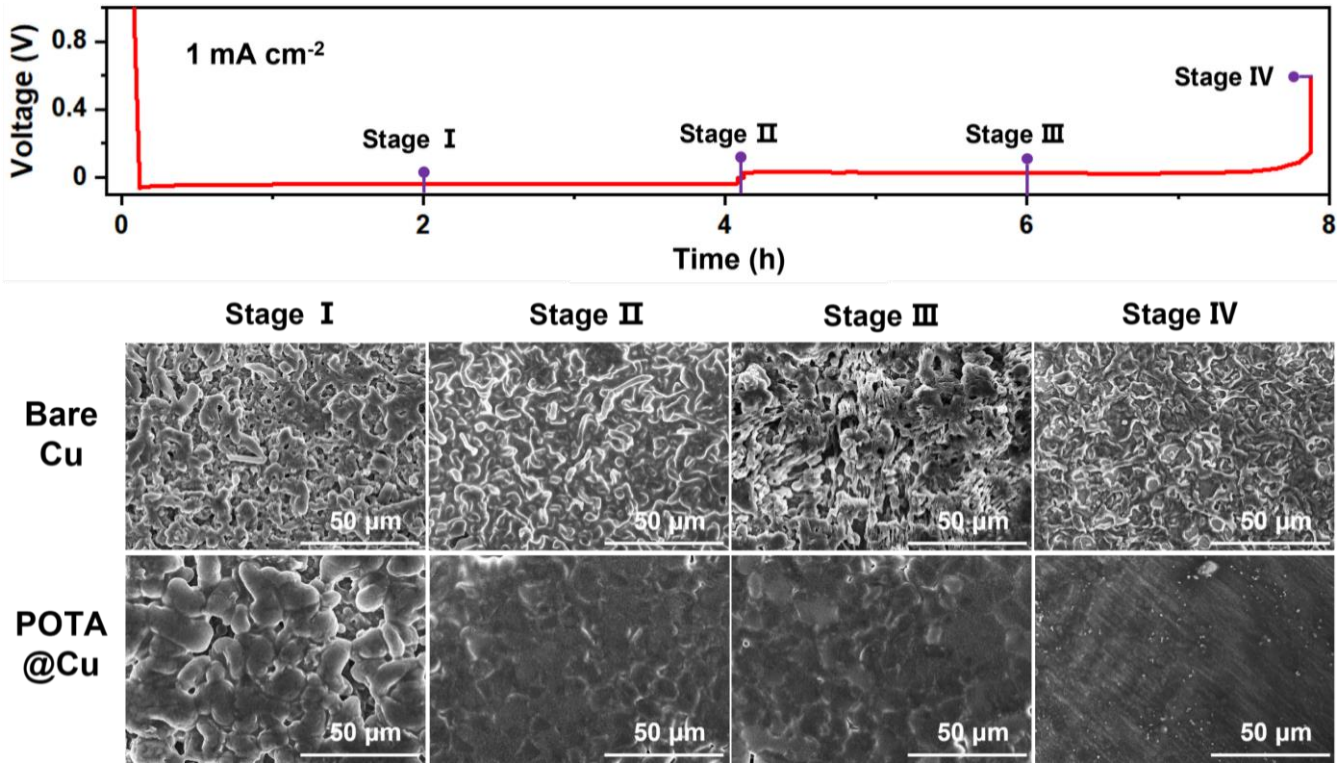

Figure S35. SEM images of Li plating onto bare Cu and POTA@Cu electrodes with 2 mAh cm^{-2} (stage I) and 4 mAh cm^{-2} (stage II) and stripping with 2 mAh cm^{-2} (stage III) and stripping completely(stage IV).

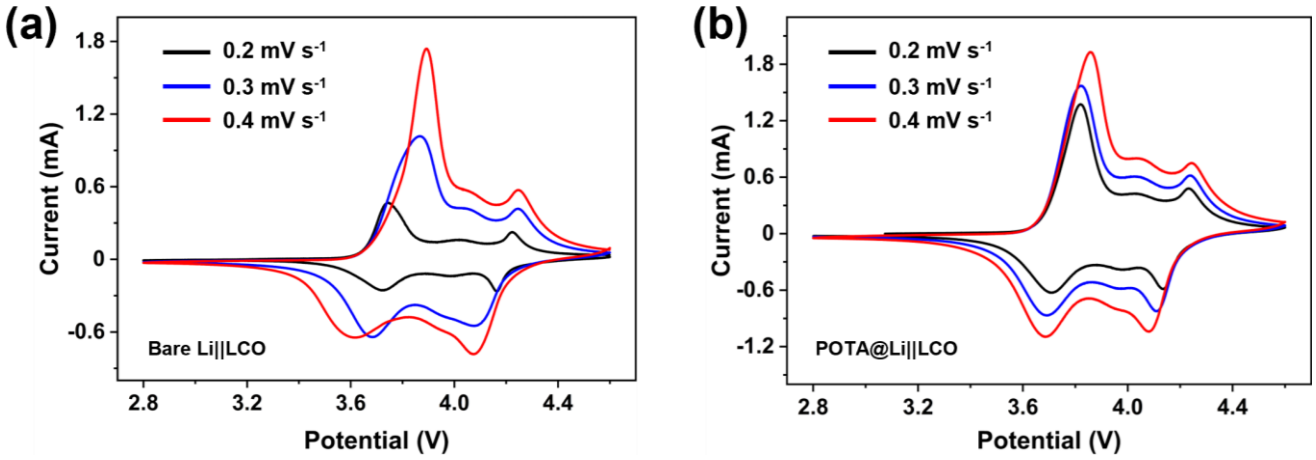

Figure S36. CV curves for (a) bare Li||LCO and (b) POTA@Li||LCO batteries at scan rates from 0.2 mV s^{-1} to 0.4 mV s^{-1}.

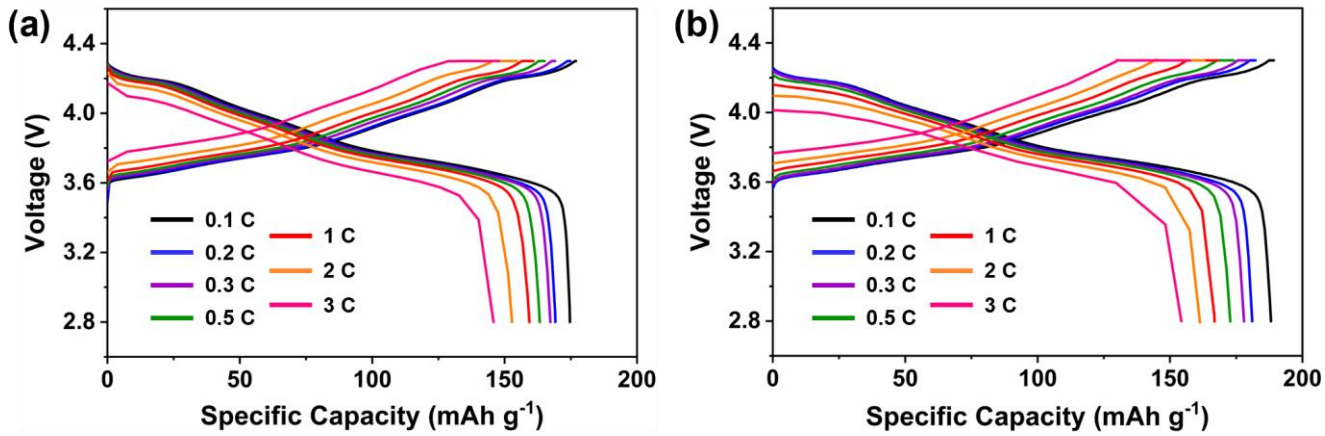

Figure S37. Voltage-capacity curves for (a) bare Li||LCO and (b) POTA@Li||LCO batteries from 0.1 C to 3 C.

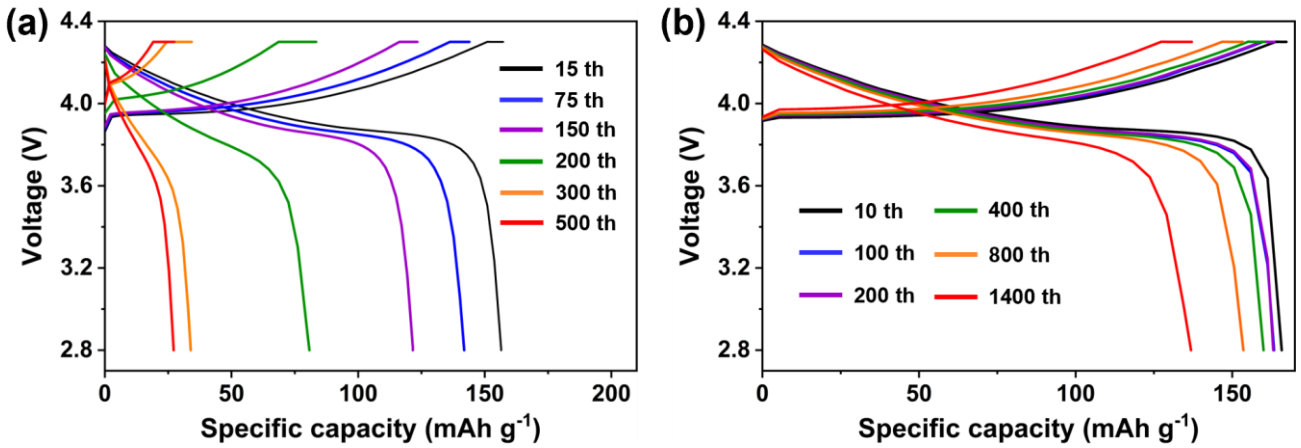

Figure S38. Voltage-capacity curves for (a) bare Li||LCO and (b) POTA@Li||LCO batteries at different cycles.

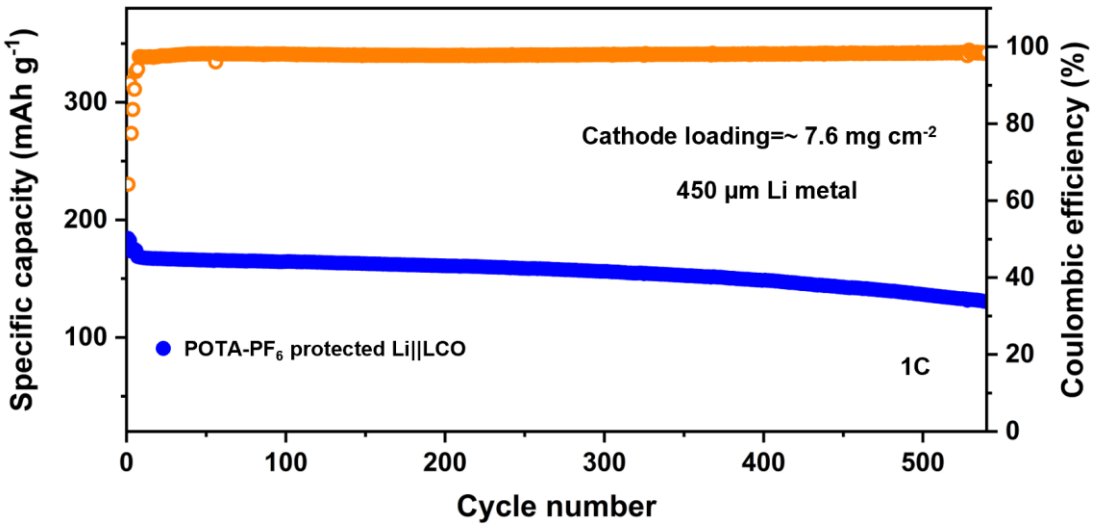

Figure S39. Cyclic performance of POTA-PF_6 protected Li||LCO at 1C.

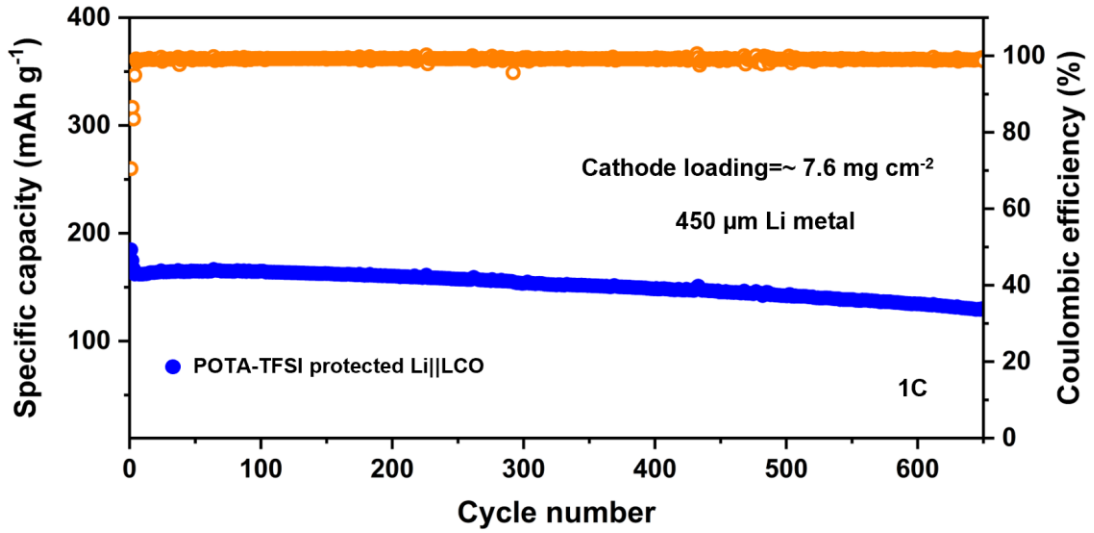

Figure S40. Cyclic performance of POTA-TFSI protected Li|| LCO at 1C.

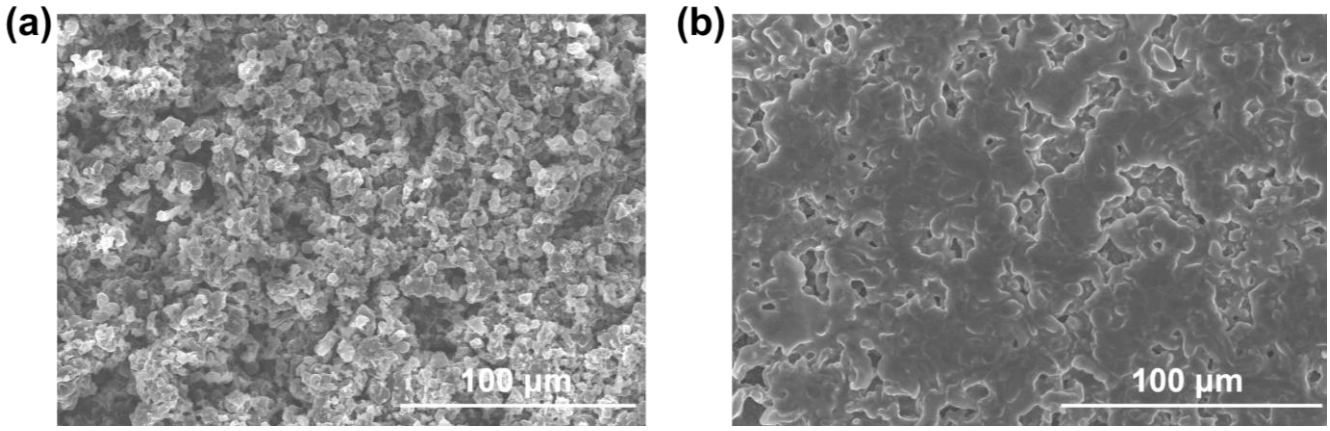

Figure S41. SEM images of (a) bare Li and (b) POTA@Li electrodes in bare Li||LCO and POTA@Li||LCO cells after 50 cycles at 1C.

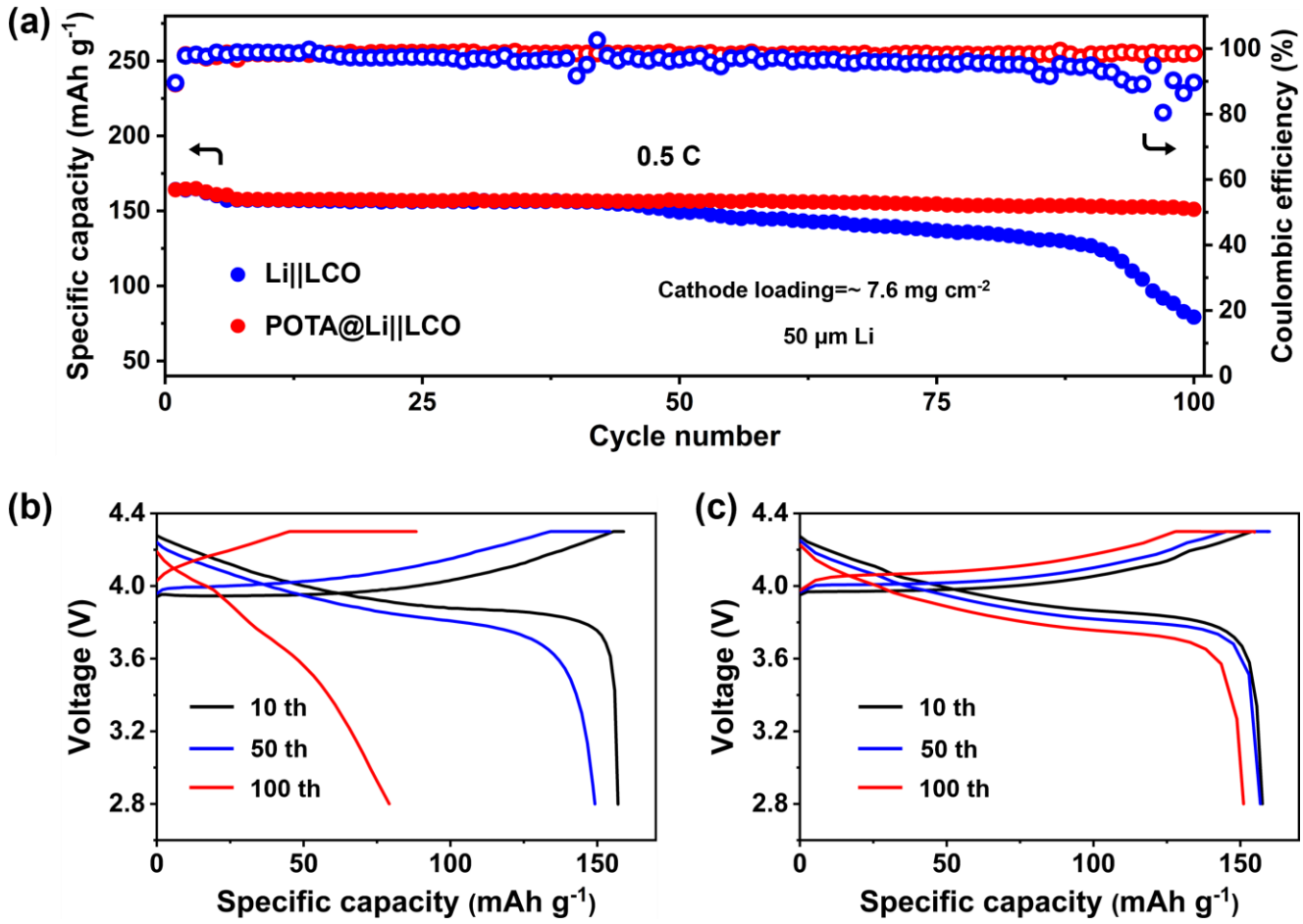

Figure S42. (a) Cycling performance of 50 μm Li||LCO cells with bare Li and POTA@Li anodes. Voltage-capacity curves for (b) bare Li||LCO and (c) POTA@Li||LCO batteries at different cycles.

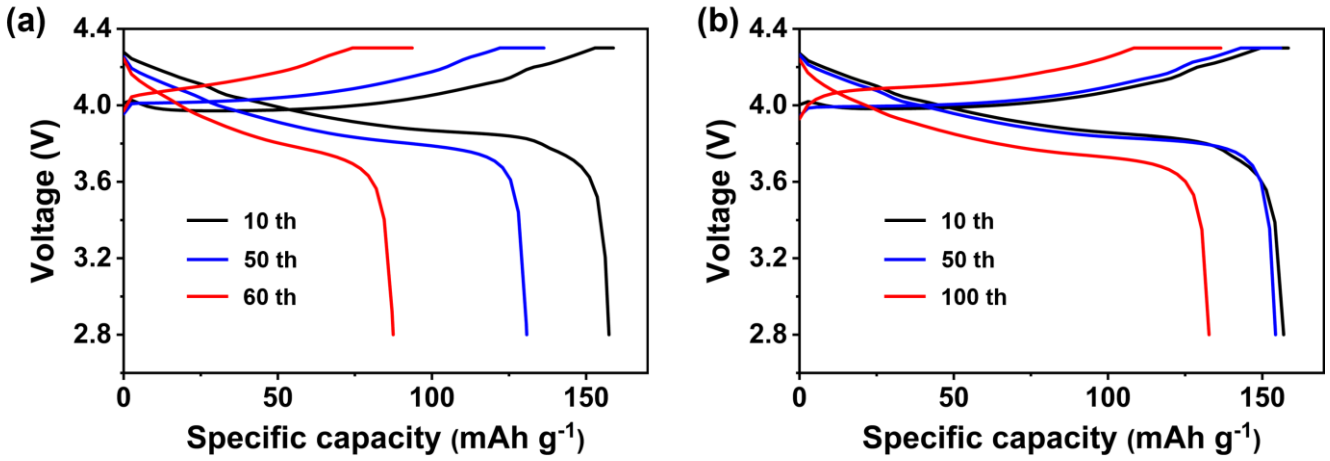

Figure S43. Voltage-capacity curves for (a) bare Li||LCO and (b) POTA@Li||LCO batteries with N/P=2.49 at different cycles.

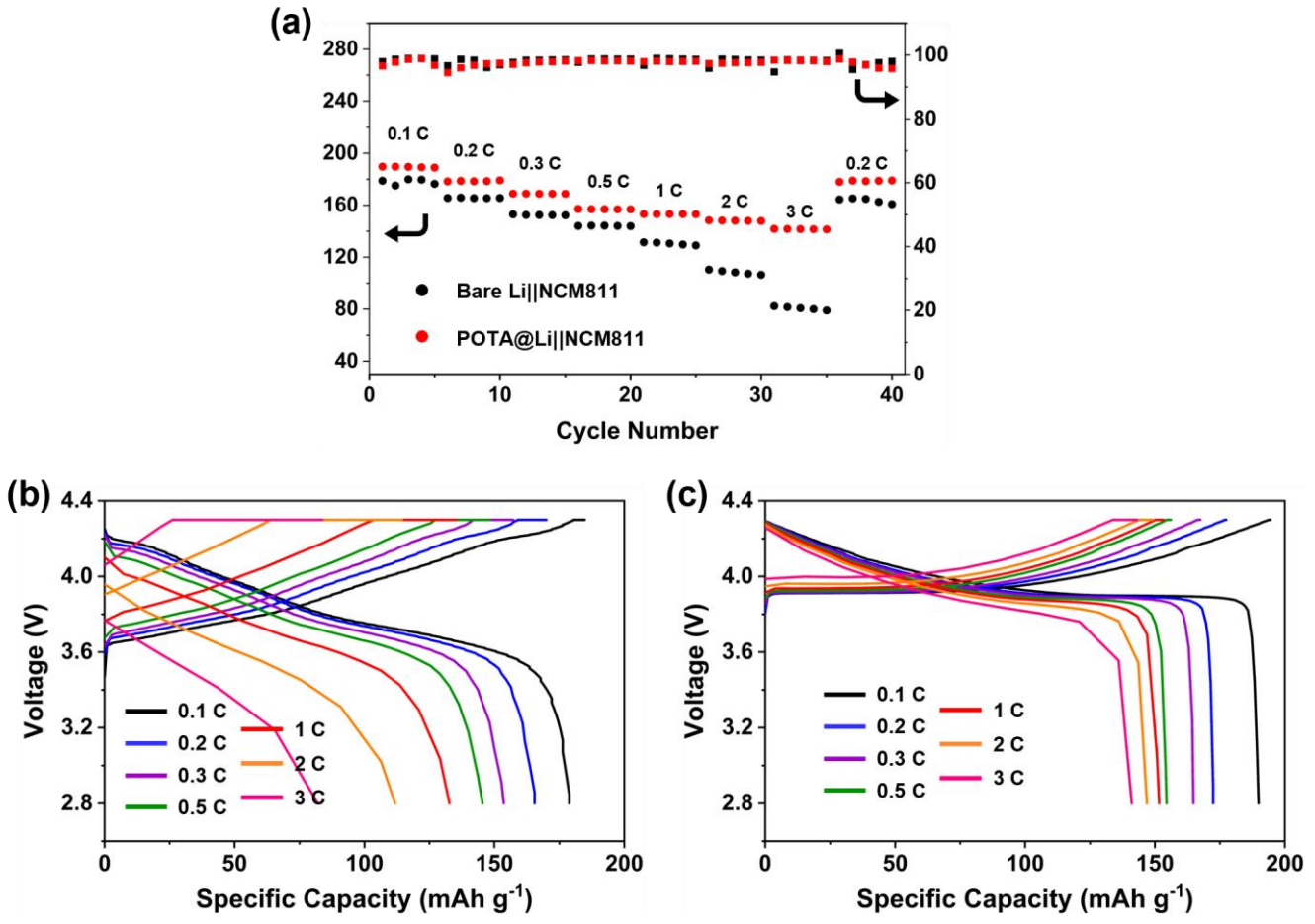

Figure S44. (a) Rate capabilities of bare Li||NCM811 and POTA@Li||NCM811 cells. Voltage-capacity curves for (b) bare Li||NCM811 and (c) POTA@Li||NCM811 batteries from 0.1 C to 3 C.

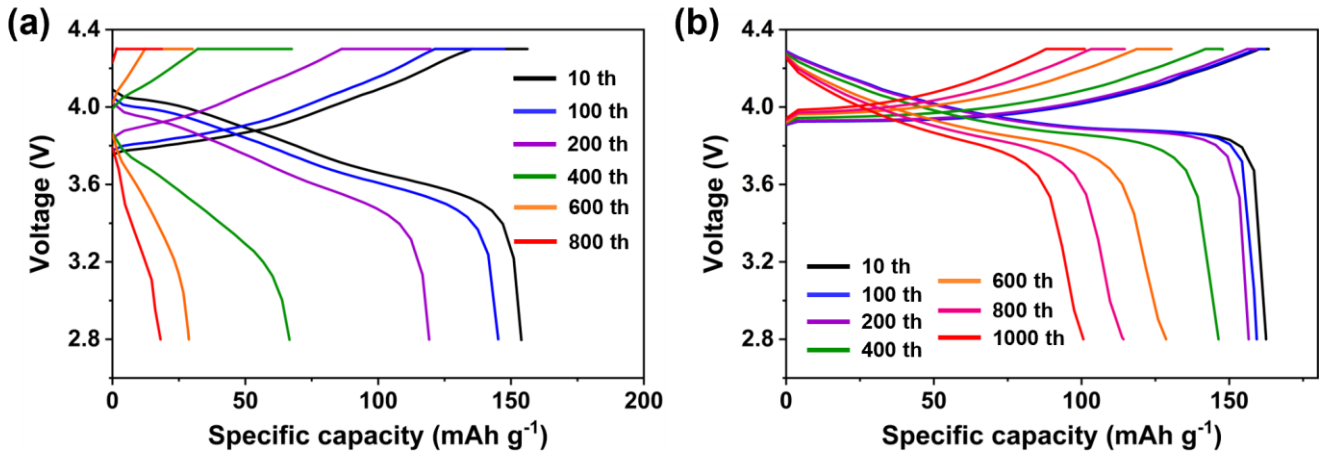

Figure S45. Voltage-capacity curves for (a) bare Li||NCM811 and (b) POTA@Li||NCM811 batteries at different cycles.

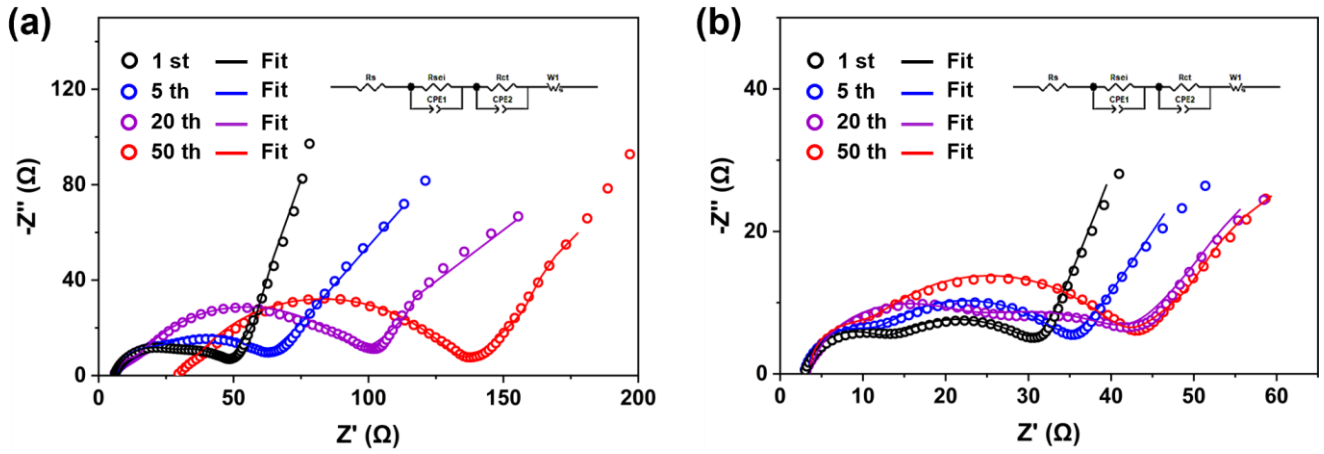

Figure S46. EIS spectrum of (g) bare Li||NCM811 and (h) POTA@Li||NCM811 cells at different cycles.

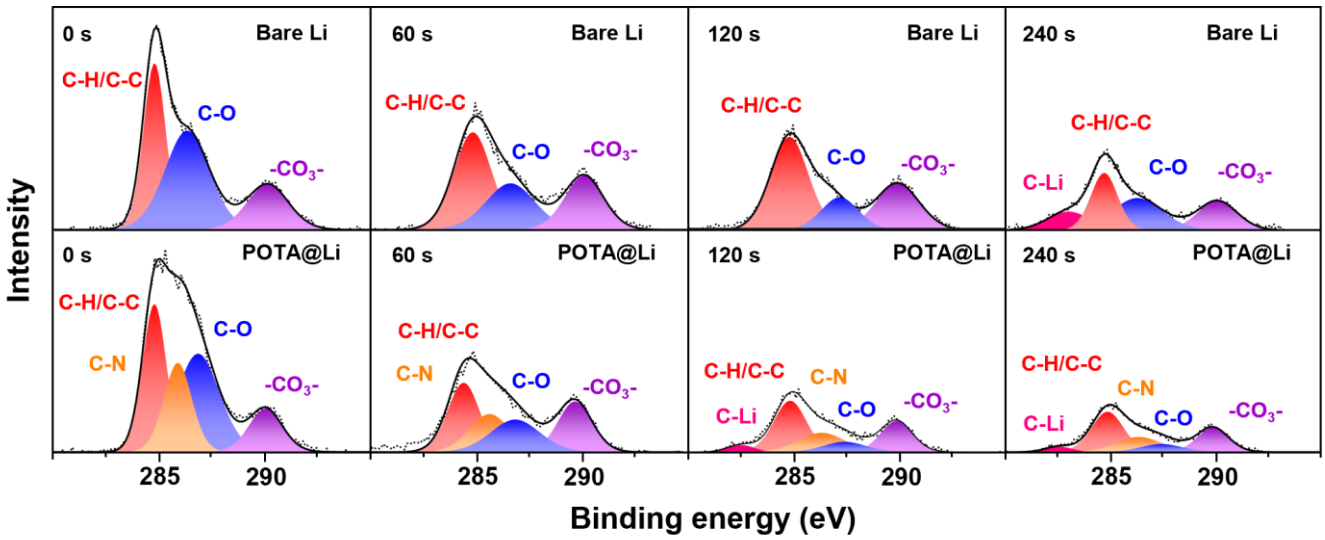

Figure S47. C1s XPS in-depth spectra of bare Li and POTA@Li electrodes in bare Li||LCO and POTA@Li||LCO cells after 20 cycles at 1C.

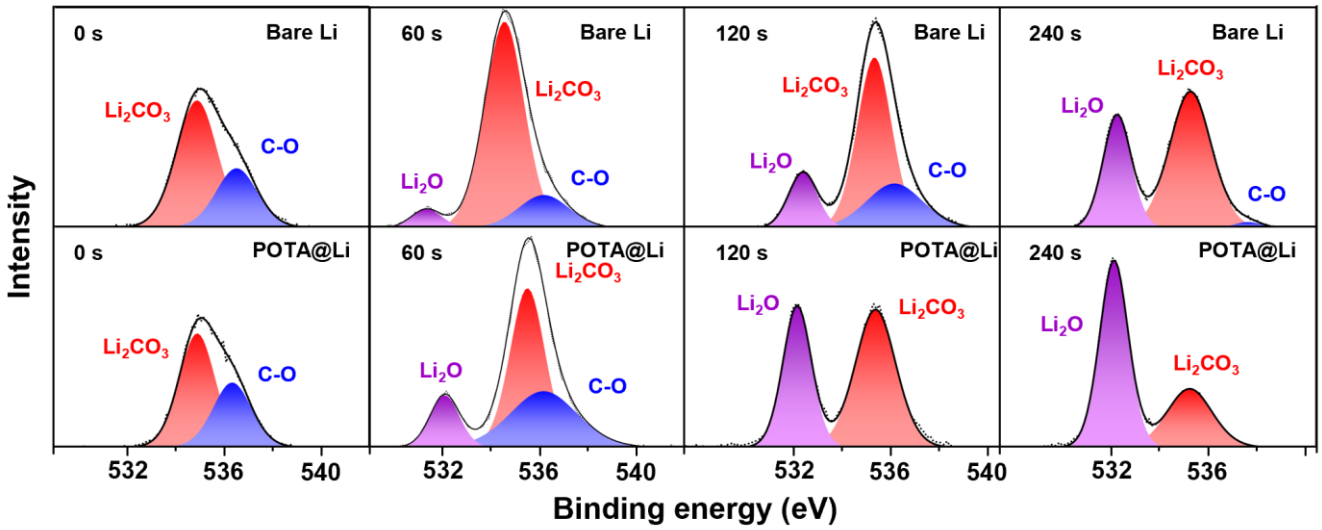

Figure S48. O1s XPS in-depth spectra of bare Li and POTA@Li electrodes in bare Li||LCO and POTA@Li||LCO cells after 20 cycles at 1C.

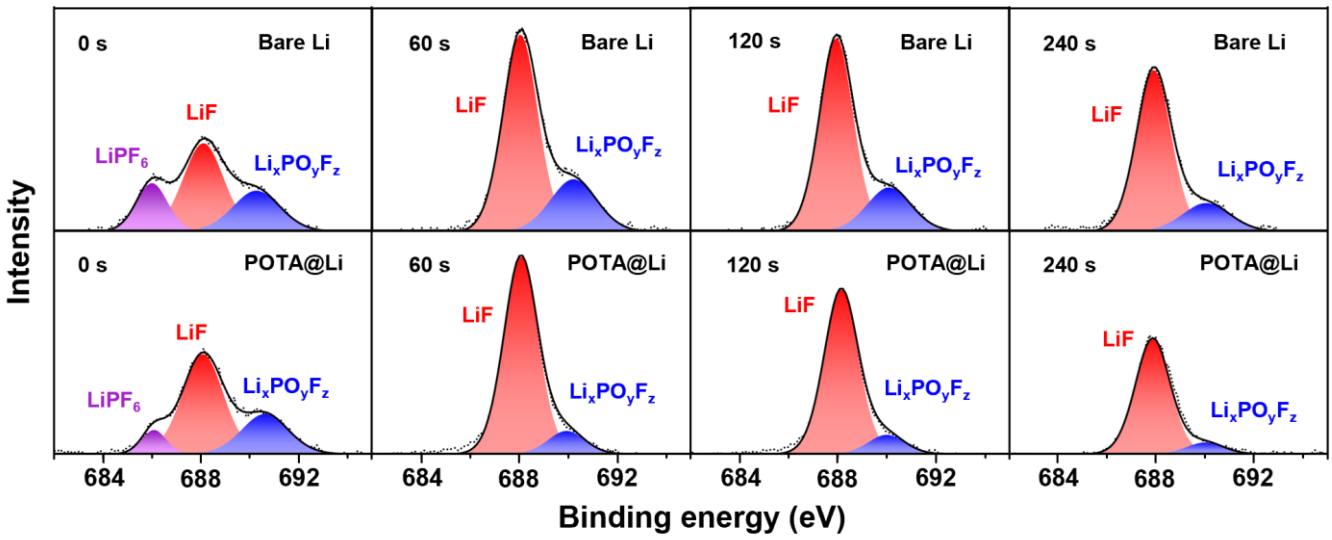

Figure S49. F1s XPS in-depth spectra of bare Li and POTA@Li electrodes in bare Li||LCO and POTA@Li||LCO cells after 20 cycles at 1C.

Table S1. Mass change data for POTA-NO_3 polymer in gel fractionation tests

Solvent	W_1 (mg)	W_2 (mg)	Xc (%)
DMSO	37.01	36.28	98.03
electrolyte solvent	41.83	41.56	99.35
H_2O	45.41	44.52	98.04
acetonitrile	44.64	43.54	97.54

Table S2. Summary of symmetric cells tests of other previous strategies.

SEI interphase	Current density (mA cm^{-2})	Area capacity (mAh cm^{-2})	Cycle time (h)	Reference
POTA-NO_3	1	1	6250	This work
	2	2	6600	
	5	5	6300	
C_3N_4 modified separator	1	1	1900	[S9]
	2	1	3000	
	5	5	2400	
$LiAlO_2$ layer	1	1	1900	[S10]
Li_xZn_y	2	2	800	[S11]
	1	1	400	
	4	2	780	
Li-B@SSM)	2	1	1200	[S12]
	1	5	840	
	3	3	450	
Cu_2S	2	2	830	[S13]
	4	4	500	
PRC-GO	1	1	1000	[S14]
	3	3	600	
PA-LiOH	3	6	300	[S15]
	5	5	1000	
P(St-Mal)	1	1	1900	[S16]
Ppy^+-PFA	1	1	500	[S17]
	2	2	500	
NO_3^--$TFSI^-$	1	1	1300	[S1]
	1	4	700	
MXene	1	1	1000	[S18]
	5	5	1000	
Li-Sn	0.5	1	2200	[S19]
	1	1	900	
LiSr	3	2	150	[S20]
	5	1	400	
SrI_2	1	1	1000	[S21]
P-PCy_3^+	1	1	1200	[S22]
CH_3OK	1	1	3500	[S23]
Li-Na	0.5	0.5	3000	[S24]
Pyr6(6) $^+$	1	1	550	[S25]
DOL-$LiNO_3$	1	0.2	2000	[S26]
TPFPB	2	2	250	[S27]

Reference

[S1] X. Wang, S. Wang, H. Wang, W. Tu, Y. Zhao, S. Li, Q. Liu, J. Wu, Y. Fu, C. Han, F. Kang, B. Li, *Adv. Mater.* 2021, **33**, 2007945.

[S2] Z. Piao, P. Xiao, R. Luo, J. Ma, R. Gao, C. Li, J. Tan, K. Yu, G. Zhou, H. M. Cheng, *Adv. Mater.* 2022, **34**, 2108400.

[S3] S. Liu, X. Ji, N. Piao, J. Chen, N. Eidson, J. Xu, P. Wang, L. Chen, J. Zhang, T. Deng, S. Hou, T. Jin, H. Wan, J. Li, J. Tu, C. Wang, *Angew. Chemie - Int. Ed.* 2021, **60**, 3661–3671.

[S4] T. D. Pham, A. Bin Faheem, J. Kim, K. Kwak, K. K. Lee, *Adv. Funct. Mater.* 2023, 2305284.

[S5] Y. Xu, L. Gao, L. Shen, Q. Liu, Y. Zhu, Q. Liu, L. Li, X. Kong, Y. Lu, H. Bin Wu, *Matter* 2020, **3**, 1685–1700.

[S6] C. Chen, Q. Liang, Z. Chen, W. Zhu, Z. Wang, Y. Li, X. Wu, X. Xiong, *Angew. Chemie - Int. Ed.* 2021, **60**, 26718–26724.

[S7] C. Zhang, J. Xie, C. Zhao, Y. Yang, Q. An, Z. Mei, Q. Xu, Y. Ding, G. Zhao, H. Guo, *Adv. Mater.* 2023, 2304511.

[S8] Z. Yu, S. Seo, J. Song, Z. Zhang, S. T. Oyakhire, Y. Wang, R. Xu, H. Gong, S. Zhang, Y. Zheng, Y. Tsao, L. Mondonico, E. G. Lomeli, X. Wang, W. Kim, K. Ryu, Z. Bao, *Adv. Energy Mater.* 2022, **12**, 2201025.

[S9] S. Dai, H. Li, B. Zhai, X. Zhi, P. Niu, S. Wang, L. Li, *Proc. Natl. Acad. Sci.* 2023, **120**, e2302375120.

[S10]K. S. Xin Hu, Yitian Ma, Ji Qian,* Wenjie Qu, Yu Li, Rui Luo, Huirong Wang, Anbin Zhou, Yi Chen, R. C. * Li Li, Feng Wu, *Adv. Mater.* 2023, 2303710.

[S11]H. J. Liu, C. Y. Yang, M. C. Han, C. Y. Yu, X. Li, Z. Z. Yu, J. Qu, *Angew. Chemie - Int. Ed.* 2023, **135**, e202217.

[S12]P. Qing, Z. Wu, A. Wang, S. Huang, K. Long, T. Naren, D. Chen, P. He, H. Huang, Y. Chen, L. Mei, L. Chen, *Adv. Mater.* 2023, **35**, 2211203.

[S13]Z. Yang, W. Liu, Q. Chen, X. Wang, W. Zhang, Q. Zhang, J. Zuo, Y. Yao, X. Gu, K. Si, K. Liu, J. Wang, Y. Gong, *Adv. Mater.* 2023, **35**, 2210130.

[S14]Y. Gao, Z. Yan, J. L. Gray, X. He, D. Wang, T. Chen, Q. Huang, Y. C. Li, H. Wang, S. H. Kim, T. E. Mallouk, D. Wang, *Nat. Mater.* 2019, **18**, 384–389.

[S15]Y. Cheng, Z. Wang, J. Chen, Y. Chen, X. Ke, D. Wu, Q. Zhang, Y. Zhu, X. Yang, M. Gu, Z. Guo, Z. Shi, *Angew. Chemie - Int. Ed.* 2023, **135**, e202305287.

[S16]T. Naren, G. C. Kuang, R. Jiang, P. Qing, H. Yang, J. Lin, Y. Chen, W. Wei, X. Ji, L. Chen, *Angew. Chemie - Int. Ed.* 2023, **62**, e2023052.

[S17]Z. Huang, S. Choudhury, H. Gong, Y. Cui, Z. Bao, *J. Am. Chem. Soc.* 2020, **142**, 21393–21403.

[S18]M. Shang, O. G. Shovon, F. E. Y. Wong, J. Niu, *Adv. Mater.* 2023, **35**, 2210111.

[S19]R. Pathak, K. Chen, A. Gurung, K. M. Reza, B. Bahrami, J. Pokharel, A. Baniya, W. He, F. Wu, Y. Zhou, K. Xu, Q. (Quinn) Qiao, *Nat. Commun.* 2020, **11**, 93.

[S20]S. Liu, X. Ji, J. Yue, S. Hou, P. Wang, C. Cui, J. Chen, B. Shao, J. Li, F. Han, J. Tu, C. Wang, *J. Am. Chem. Soc.* 2020, **142**, 2438–2447.

[S21]L. Dong, S. Zhong, B. Yuan, Y. Li, J. Liu, Y. Ji, D. Chen, Y. Liu, C. Yang, J. Han, W. He, *Angew. Chemie - Int. Ed.* 2023, **135**, 2301073.

[S22]A. S. Han, B. Wu, H. Wang, P. Wen, X. Lin, M. Chen, *Angew. Chemie - Int. Ed.* 2023, **135**, 2308724.

[S23]J. Yang, M. Li, Z. Sun, X. Lian, Y. Wang, Y. Niu, C. Jiang, Y. Luo, Y. Liu, Z. Tian, Y. Long, K. Zhang, P. Yu, J. Zhang, Z. Wang, G. Wu, M. Gu, W. Chen, *Energy Environ. Sci.* 2023, **16**, 3837-3846.

[S24]Y. Wang, F. Liu, G. Fan, X. Qiu, J. Liu, Z. Yan, K. Zhang, F. Cheng, J. Chen, *J. Am. Chem. Soc.* 2021, **143**, 2829–2837.

[S25]J. Jang, J. S. Shin, S. Ko, H. Park, W. J. Song, C. B. Park, J. Kang, *Adv. Energy Mater.* 2022, **12**, 2103955.

[S26]Q. Zhao, X. Liu, J. Zheng, Y. Deng, A. Warren, Q. Zhang, L. Archer, *Proc. Natl. Acad. Sci. U. S. A.* 2020, **117**, 26053–26060.

[S27]S. Li, W. Zhang, Q. Wu, L. Fan, X. Wang, X. Wang, Z. Shen, Y. He, Y. Lu, *Angew. Chemie - Int. Ed.* 2020, **59**, 14935–14941.